EFFECTS OF MICROSTRUCTURE ON THE INTERNAL HYDROGEN EMBRITTLEMENT OF A 4340 STEEL

Charles Edward Bauer
B.S., Stanford University, 1972
M.S., Ohio State University, Columbus, 1975

A dissertation submitted to the faculty
of the Oregon Graduate Center
in partial fulfillment of the
requirements for the degree
Doctor of Philosophy
in
Materials Science and Engineering

May, 1980

The dissertation "Effects of Microstructure on the Internal Hydrogen Embrittlement of a 4340 Steel" by Charles Edward Bauer has been examined and approved by the following Examination Committee:

William E. Wood, Research Advisor
Associate Professor

Nicholas G. Eror
Associate Professor

Jack H. Devletian
Associate Professor

Lynwood W. Swanson
Professor

DEDICATION

This dissertation is dedicated to G. Marshall Pound, Professor, Stanford University, without whose encouragement and counsel I would not have pursued a graduate program in the science of materials.

TABLE OF CONTENTS

LIST OF FIGURES

Page

LIST OF TABLES

ABSTRACT

Effect of Microstructure on the Internal Hydrogen Embrittlement of a 4340 Steel

Charles Edward Bauer, Ph.D.
Oregon Graduate Center, 1980

Supervising Professor: William E. Wood

Hydrogen-assisted delayed brittle fracture of high strength, low alloy steels is highly dependent on microstructure. Several specific microstructural features were observed to significantly alter both the static and dynamic resistance to hydrogen-assisted cracking of a 4340 steel. Increasing grain size increased both the threshold stress intensity (K_{th}) and the Stage II crack growth rate. More homogeneous distribution of impurities such as P and S increased K_{th} but hardly affected Stage II crack growth rate. And a fine dispersion of retained austenite platelets greatly improved both K_{th} and Stage II crack growth rate.

Sensitivity of K_{th} to hydrogen concentration was found to be greatest below approximately 2 ppm nascent hydrogen while above 2 ppm $\underline{H}$ K_{th} became relatively independent of hydrogen concentration. Although not observed at hydrogen levels below 2 ppm, Stage II crack growth rates did not show sensitivity to hydrogen concentration.

INTRODUCTION

A. General Characteristics of Hydrogen Embrittlement

Sustained load cracking at low stress intensity levels typifies internal hydrogen embrittlement in low alloy steels heat treated to high strength levels. At or near a crack tip, hydrogen exerts an embrittling effect that leads to intergranular, transgranular, or mixed mode fracture,[1] all of which exhibit drastically reduced macroscopic ductility. Proposed mechanisms include a decohesion model,[2-10] dislocation mobility[11-16] and surface energy considerations,[17,18] stress-sorption[19,20] and planar pressure theories.[21-26]

The primary concern of this treatise is the hydrogen-induced delayed brittle fracture of high strength steels. However, the general characteristics of hydrogen embrittlement phenomena will shed light on later discussions. These characteristics are summarized as follows:[2,16,18,27,28]

1. Hydrogen apparently has no effect on elastic properties and hardness values.
2. Hydrogen embrittlement occurs between approximately -100°C and +100 °C with the most deleterious effects being near room temperature (20°C).

3. Hydrogen embrittlement is highly sensitive to strain rate, the effect being greatest at low strain rates.
4. In general, susceptibility to hydrogen embrittlement increases with increasing tensile strength, heat treatable high strength martinsitic steels being most sensitive.
5. The severity of hydrogen embrittlement increases as stress concentration increases; i.e., as the crack tip radius decreases.
6. At least initially, increases in hydrogen content lead to decreases in both the threshold stress intensity and the ductility to failure.

B. Historical Summary, Proposed Mechanisms

The embrittling effect of hydrogen in steel has been documented since the late 1800's when Johnson[29] found "that iron wire became more brittle after a few minutes immersion in strong hydrochloric or dilute sulphuric acid--a piece breaking after being bent once on itself, while before immersion it would bear bending on itself and back again two or three times before breaking."[29] Later investigation showed reduced ductility,[30] decreased fracture stress,[31,32] and susceptibility to delayed brittle fracture.[33-35]

The earliest theories for the mechanism of hydrogen embrittlement took the ductility drop to be due to the strain hardening effects of an

iron hydride formation.[36] Lack of any evidence,[37] thermodynamic or otherwise, for the existence of an iron hydride led to the elimination of this model for the case of high strength steels.

Establishment of solubility-pressure-temperature relationships for hydrogen in steel led to the suggestion that very high pressures would be created in internal voids when hydrogen was thrown out of solution during quenching from higher temperatures. This high hydrogen pressure in voids then increases as more hydrogen precipitates until a critical pressure is reached at which the metal lattice is "sprung apart"[22-24] by the hydrostatic forces of the gas. If a stress is then applied, premature fracture occurs. However, this "planar pressure" theory does not account for either the strain rate dependence or the reversibility of hydrogen-induced delayed brittle fracture.

Later theories considered the effects of gaseous hydrogen on propagation of Griffith type cracks.[17,20,38] The basic mechanism of a Griffith crack postulates that all materials, especially brittle metals, contain microscopic or submicroscopic cracks which can propagate catastrophically when a critical stress intensity is exceeded. Whether or not the crack grows is governed by the balance between the increase in surface energy due to crack growth and the decrease in strain energy of the surrounding material if the crack grows. When this balance is such that the energy released by extension of the crack is greater than the energy required to create the new surface of the enlarged region of the crack, rapid crack propagation will occur.[39,40]

De Kazinczy[20] suggested that the presence of hydrogen gas within the microcracks adds an additional term to the Griffith energy balance; i.e., the energy of the gas itself, released during adiabatic expansion as the crack propagates.

Petch[17,38] proposed that atomic hydrogen absorbs on the surfaces of the Griffith microcracks, thus lowering the surface energy and correspondingly increasing the free energy available for crack propagation. Uhlig[19] proposed a similar model in relation to stress corrosion cracking.

The key to both the de Kazinczy and the Petch models is that hydrogen alters the thermodynamics of crack propagation. De Kazinczy states that hydrogen increases the energy released during crack propagation while Petch argues that hydrogen decreases the energy required to form a new surface.

Van Leeuwen,[41-45] Williams and Nelson,[46,47] and Tetelman[48] have contributed to the refinement of the stress-sorption, planar pressure theories of hydrogen embrittlement, the essential elements of which have been presented above.

Bastien and Azou[11] were the first to suggest hydrogen might be transported by and interact with dislocations. Tien[49] showed how hydrogen can be transported by dislocations, and Louthen et al[12,15] showed how hydrogen might be absorbed and transported in the metal lattice during plastic deformation. Subsequently, Lynch and Ryan[13] proposed that hydrogen assists dislocation generation at crack tips by decreasing

the crack tip surface tension. Beachem[16] added that hydrogen might ease the flow of dislocations[50] through a similar action ahead of a crack tip, thus localizing plastic flow.

In 1959, A. R. Troiano[2] summarized his and his coworkers[4-6] results and presented a unified decohesion theory of internal hydrogen-assisted cracking. In this theory, electrons contributed by the dissolved hydrogen would modify the d-electron bonds of the iron atoms such that the cohesive bonding energy of the lattice was decreased. If a sufficient concentration of hydrogen was concentrated in a localized area, then a significantly lower applied stress intensity would be required to initiate and propagate a crack. Steigerwald,[3,5,18] Oriani,[7-10] and Gerberich et al[51-55] have investigated various aspects of the decohesion model and concluded that atomic hydrogen migrates to a crack tip under the influence of a triaxial stress[56] where it exerts an embrittling effect.

C. Availability and Mobility of Hydrogen

Regardless of the mechanism of embrittlement, the amount of and mobility of diffusable atomic hydrogen plays a key role in the hydrogen-induced delayed brittle failure of high strength, low alloy steels.[2,7,49,53,57] The microstructure of BCC steel strongly influences mobility of dissolved hydrogen. In Coe and Martin's[58] review of microstructural effects on apparent hydrogen diffusivity in steel, they found that iron

carbide present in globular form allows apparent diffusivity one order of magnitude greater than when the carbides form a coarse pearlite structure. Others have shown that martensite and lower bainite have the lowest diffusivities, apparently due to finely dispersed auto-tempered carbides in the strained lattice.

McNabb and Foster[59] developed a model assuming hydrogen to be delayed at specific sites in the lattice due to the presence of potential wells significantly deeper than those encountered in normal regions of a crystal lattice. Oriani[60] expanded on this model to show that dissolved hydrogen is trapped or delayed even when it diffuses within a small distance of a trap. Using a similar trapping model, Evans and Rollason[61] studied the effects of voids on apparent hydrogen diffusivity in a high sulphur-free cutting steel and concluded that apparent diffusivity could be decreased by an order of magnitude through a trapping mechanism. Koiwa[62] also studied trapping of interstitials in BCC metals and found similar behavior.

Several investigators have suggested that trapping of hydrogen at specific sites in the lattice should improve resistance to hydrogen-induced delayed cracking by immobilizing the atomic hydrogen.[54,63-70] Kortovich[63] showed that rare earth additions of cerium and lanthanum in AISI 4340 steel led to increased threshold stress intensities and lower crack growth rates in cathodically charged specimens. Cadeño[70] and Ritchie et al[65] found that a silicon-modified 4340 steel containing significant quantities of retained austenite exhibited reduced crack

growth rates when compared with an unmodified 4340 alloy. However, they found that the threshold stress intensities remained relatively unchanged.

The current study discusses relationships between precisely measured hydrogen concentrations, threshold stress intensities, and hydrogen-assisted crack growth rates for different microstructures of an AISI 4340 steel. These data are explained in terms of the roles of microstructure, possible trapping sites, and thermodynamics of the hydrogen-induced delayed brittle cracking of high strength, low alloy steels.

EXPERIMENTAL PROCEDURES

A. Material and Specimen Design

The material studied was fully annealed aircraft quality AISI 4340 steel with the analyzed composition shown in Table I. The as-received material was machined into bolt-loaded double cantilever beam (DCB) specimens, shown in Figure 1, for threshold stress intensity study. Compact tension specimens (CTS), shown in Figure 2, were also machined from the same material for crack growth rate investigation.

B. Specimen Cleaning and Degassing

Subsequent to the machining operations, all samples were degreased with acetone and then vacuum annealed at 400°C for eight (8) hours at a pressure of 10^{-7} torr in a continuously ion-pumped system. This baking operation assured a constant baseline hydrogen content for all samples prior to heat treatment.

C. Heat Treatment Procedures

Heat treatment schedules (see Table II) included a one (1) hour solution treatment in an argon atmosphere at either 870°C or 1200°C

followed by direct oil quenching to room temperature. A step quenching procedure consisting of solution treatment at 1200°C for one (1) hour followed by a furnace quench to 870°C for one-half (1/2) hour prior to direct oil quenching was also employed. A schematic drawing of the solution treating furnace is shown in Figure 3. Salt bath tempering for one (1) hour at either 180°C or 280°C followed each solution treatment. The tensile and K_{IC} data[80] are presented in Table III along with the general microstructural features for each heat treatment investigated in Table IV.

D. Charging and Plating

Following heat treatment, all samples were polished on a 120 grit wheel and cathodically charged with hydrogen at 25°C in a 4 percent sulphuric acid bath containing a poison consisting of one (1) gram yellow phosphorus dissolved in 20 milliliters of carbon disulphide(CS_2). Each sample was charged in a fresh bath which contained 600 milliliters of the acid solution and ten (10) milliliters of the poison mixture. The charging current density was 14 milliamps per square centimeter and the charging time was varied from six (6) hours to 48 hours to facilitate varying degrees of hydrogen occlusion in the test samples.

Immediately following the charging operation, each specimen was hand-polished on all surfaces using 300 grit emery cloth and ultrasonically cleaned for ten (10) minutes in a 10 percent hydrochloric acid (HCl) solution. After thorough rinsing, the specimens were bright

cadmium plated in a cyanide plating bath at a current density of 1.5 amperes per square centimeter for ten (10) minutes. The purpose of the bright cadmium plate was to trap the cathodically charged hydrogen within the specimens.

E. Threshold Testing and Acoustic Emission Detection

Subsequent to a 24-hour aging period, the DCB specimens were bolt-loaded to a constant crack opening displacement to initiate the threshold stress intensity level test. The delayed hydrogen-induced cracking was monitored at 25°C using an AET Model 201 acoustic emission detection system. The acoustic emission testing established that 50 to 75 hours was sufficient to achieve crack arrest; i.e., no acoustic emission was detected at longer times. Therefore, the DCB specimens were left under load for 100 hours to assure achievement of crack arrest, at the threshold stress intensity level, before being fast-fractured to the end of the specimen. Crack length "a" at the point of crack arrest was determined with a Gaertner cathatometer and several samples weighing between one (1.0) gram and 2.5 grams were immediately sectioned from each specimen (see Figure 1) and stored in liquid nitrogen until the dissolved hydrogen (H) content was determined.

F. Crack Growth Rate Testing

All CTS specimens were cathodically charged for 48 hours and aged 24 hours after cadmium plating prior to testing in the dead weight frame and monitoring system shown schematically in Figure 4. Following the aging period, each CTS specimen had an 0.008 inch wide slot ground into the base of the notch (see Figure 2) to establish a sharper initial crack tip radius. The CTS specimen would then be loaded, to a stress intensity level of approximately 50 percent of the K_{IC} stress intensity for the particular heat treated microstructure being tested, for about 15 minutes. This preloading step was employed to initiate a sharp crack prior to crack growth rate investigation. Finally, the CTS specimens were loaded so as to produce a stress intensity level as close to the threshold stress intensity level as possible. Crack growth was monitored as a function of time using an Instron crack opening displacement gauge in conjunction with an AET time base generator. Immediately upon final fracture of each CTS specimen, several samples were sectioned from each specimen (see Figure 2) and stored in liquid nitrogen for subsequent hydrogen analysis.

G. Hydrogen Analysis

The occluded hydrogen measurements were conducted utilizing an "Ultrasensitive Hydrogen Analysis System" developed by K. B. Das[71,72]

The system works on the principle of selective permeation of hydrogen through a semipermeable metallic membrane. This instrument allows the measurement of hydrogen content in the range of a few parts per billion by weight in a carrier gas stream of argon and is proven to have the capability of measuring relative hydrogen contents in metals of the order of a few tenths parts per million by weight (ppm) with an accuracy of better than plus or minus 10 percent. This unique capability was necessary for hydrogen measurements in this study since the presence of only a few ppm nascent hydrogen can embrittle high strength steels.[2,53,73] Details of operating procedure, range, and accuracy of the instrument are described elsewhere.[72]

H. Fractography

SEM fractographs were taken as a function of applied stress intensity employing a JEOL scanning electron microscope at a secondary accelerating voltage of 20 kV.

RESULTS

A. Hydrogen Content and Charging

Figure 5 shows dissolved hydrogen content as a function of charging time for microstructure A. Although hydrogen pick-up tended to increase with increasing charging time in general, the scatter in the data clearly shows why one should not make an attempt to predict accurate hydrogen levels based on charging time alone. This ambiguity points out the danger inherent in the application of calculated hydrogen concentrations to studies of internal hydrogen-induced cracking.

B. Threshold Stress Intensities and Microstructure

Threshold stress intensity values (K_{th}) were determined using the relation[74]

$$K_{th} = \frac{VEh\ 3h(a + 0.6h)^2 + h^3}{4\ (a + 0.6h)^3 + h^2 a}^{1/2} \qquad (I)$$

where "V" is the crack opening displacement, "E" the Young's modulus, "h" the half height of the specimen, and "a" the crack length from the line of loading. Data plotted in Figure 6 for dissolved hydrogen content versus threshold stress intensity showed that the correlation of

K_{th} with bulk hydrogen content was very consistent with a low scatter level. It should be noted that because of some scatter in the hydrogen data, the hydrogen contents reported in Figure 6 are the average of at least three measurements per specimen. As can be seen, for all heat treatments, sensitivity to hydrogen-induced cracking essentially disappeared at hydrogen levels below approximately 1 ppm. The extreme sensitivity of K_{th} to small changes in hydrogen content between 1 ppm and 2 ppm emphasizes the critical nature of internal hydrogen embrittlement and importance of hydrogen measurements in such studies. At hydrogen levels greater than 2 ppm, an apparent "baseline" threshold stress intensity value was attained; i.e., the K_{th} values became essentially independent of bulk hydrogen content above 2 ppm occluded hydrogen.

The significant microstructural features produced by the various heat treatment schedules are found in Table IV[75-78] along with the corresponding K_{IC} and "baseline" K_{th} values. Optical photomicrographs of heat treatments A and E in Figure 7 show the difference in grain size produced by the 1200°C and 870°C solutioning treatments. The TEM photomicrographs in Figure 8a show the presence of retained austenite[79] as thin films on lath boundaries in microstructure A. Figures 8b and 8c show the absence of significant amounts of retained austenite in microstructures B and E,[79] respectively. Kahn et al[79] and Wood et al[77,78] have also shown that direct quenching from 1200°C results in a microstructure that displays little twinning while step quenching from 1200°C to 870°C and direct quenching from 870°C result in extensively twinned microstructures.

Evidence for segregation of impurities such as phosphorus and sulfur has been collected by McMahon et al.[80-84] And Clark et al[85] have shown indirect evidence for a model of phosphorus and sulfur segregation similar to that implied in this work.

Microstructures E and F each showed baseline K_{th} values of 12 MPa$\sqrt{m}$ and revealed that small changes in the tempered carbide structure had little or no effect on the mechanics of hydrogen embrittlement. Heat treatments A and B showed baseline threshold values of 30 MPa$\sqrt{m}$ and 21 MPa$\sqrt{m}$, respectively, a difference in threshold stress intensity value of approximately 9 MPa$\sqrt{m}$. The only difference in microstructure was the presence of retained austenite in microstructure A, while in heat treatment B, the 280°C temper transformed the retained austenite. For microstructures C and D, baseline K_{th} values of 26.5 MPa$\sqrt{m}$ and 17.5 MPa$\sqrt{m}$ were found. Again, the presence of retained austenite led to an increase of 9 MPa$\sqrt{m}$ in the baseline threshold stress intensity. This tends to indicate that the presence of retained austenite definitely improves the threshold stress intensity values in hydrogen charged specimens. Presence of twinning and/or segregation to grain boundaries in the microstructure appears to decrease the K_{th} values by approximately 3.5 MPa$\sqrt{m}$ when the specimens A,B and C,D are compared at a given hydrogen level. However, in the succeeding discussion, it will be shown that twinning does not play any part in this decrease.

An increased resistance to hydrogen-induced cracking with increased grain size was found by comparing microstructures D and F. The magnitude of the increase in the K_{th} value was approximately 5.5 MPa$\sqrt{m}$ for an

increase in grain diameter from 15-20 microns for microstructure F to a grain diameter of 150-200 microns in microstructure D.

Comparison of the microstructures produced by heat treatments A and C, or B and D revealed two possibly interrelated significant differences: first, the presence or absence of extensive twinning of the martensitic phase and second, the distribution of trace impurities such as phosphorus and sulphur.[83-85] Heat treatments A and B resulted in a dislocated lath martensite containing few twins and a relatively "homogeneous" distribution of P and S impurities, suggested by Clark.[85] On the other hand, microstructures C and D were extensively twinned and phosphorus and sulphur were segregated at grain boundaries.[83,84] Twinning of the martensite would not be expected to play a significant role in the hydrogen-induced delayed brittle cracking of this steel since hydrogen-induced cracking at threshold stress intensity levels in 4340 steel was almost exclusively by intergranular fracture (see Figure 9) and twins or twin packets operating as crack nucleation sites would have led to significant amounts of transgranular cleavage-type fracture. Thus, a more homogeneous impurity distribution appears to increase the baseline threshold stress intensity of this steel by approximately 3.5 $MPa\sqrt{m}$.

The microstructural manipulations employed in the present work contributed to increased resistance to hydrogen-induced delayed brittle fracture in the following amounts: Retained austenite increased baseline K_{th} by approximately 9 $MPa\sqrt{m}$, increased grain diameter from 15-20

microns to 150-200 microns, increased baseline K_{th} by approximately 5.5 MPa$\sqrt{m}$, and increased homogeneity of impurity distribution (most probably P and S) led to an increase in baseline K_{th} of approximately 3.5 MPa$\sqrt{m}$.

C. Crack Growth Rates, Applied Stress Intensity and Microstructure

Figures 10 through 15 present the hydrogen-assisted crack growth rate ($\frac{da}{dt}$) as a function of the applied stress intensity for each microstructure investigated. All specimens displayed the same "three stage" crack growth rate dependence on applied stress intensity as noted by Gerberich et al.[51-55] Stage I (see Figure 10) represents the threshold stress intensity where crack growth rate was essentially nil below K_{th}. During Stage II, crack growth rate became relatively independent of the applied stress intensity and Stage III resulted in increasing crack growth rates as the plane strain fracture toughness of the material (K_{IC}) is approached.

Since the hydrogen content of each specimen was greater than two (2) parts per million (see Table V), Stage I crack growth rate was negligible near the baseline threshold stress intensity level determined from the DCB specimens for each microstructure. Also, the Stage III crack growth rates approached the catastrophic level as the plane strain fracture toughness of the specimen was approached.

In Figure 16, the Stage II crack growth rate for each heat treatment schedule is shown as a function of the applied stress intensity.

Note that the range of applied stress intensities over which Stage II crack growth occurred was limited but not necessarily determined by the relative values of the baseline threshold stress intensity and the plane strain fracture toughness of each specimen, while the Stage II crack growth rate was controlled by the microstructure of each specimen.

Comparison of microstructures E and F (see Table VI) revealed that small changes in the tempered carbide structure had a strong effect on the kinetics of hydrogen-assisted crack growth. The larger, more extensive carbides produced by the 280°C temper apparently decreased the hydrogen-assisted Stage II crack growth rate by a factor of four (4).

Microstructures A and C showed the lowest Stage II crack growth rates of approximately 3.5×10^{-6} in. sec.$^{-1}$ and revealed that the impurity redistribution previously shown to have improved the baseline threshold stress intensity had no significant effect on the hydrogen-assisted crack growth kinetics of the AISI 4340 alloy.

A comparison of microstructures D and F with respect to Stage II crack growth rate shows the 870°C quenched and 280°C tempered (F) Stage II crack growth rate to be superior to an identically tempered step quenched specimen (D) by a factor of ten (10). This implies that similar specimens tempered at 180°C, but not containing retained austenite, would display a Stage II crack growth rate of approximately 1.5×10^{-4} in. sec.$^{-1}$, since the carbide tempering reaction appears to be relatively independent of the solutioning temperature for this alloy. Therefore, the increased grain size (150-200 microns diameter) produced by the 1200°C solution treatment apparently increases the Stage II crack

growth rate of the present alloy by one order of magnitude.

Microstructures B and D showed Stage II crack growth rates of 2.8×10^{-5} in. sec.$^{-1}$ and 4.0×10^{-5} in. sec.$^{-1}$, respectively. Comparison with microstructures A and C disclosed the value of retained austenite for improved properties with respect to hydrogen-assisted cracking in the present alloy. Retained austenite not only increased the baseline threshold stress intensity, but also decreased Stage II crack growth rates. The magnitude of this Stage II crack growth rate decrease was at least one order of magnitude, and considering the detrimental effect of the increased grain size, the true contribution of retained austenite was a two (2) order of magnitude decrease in the Stage II hydrogen-assisted crack growth rate of this AISI 4340 steel.

The effects of the present microstructural variations on the hydrogen-assisted Stage II crack growth rates of AISI 4340 steel were as follows: Increased grain diameter of an order of magnitude (from 15-20 microns to 150-200 microns) also increased the Stage II crack growth rate by an order of magnitude (from 4.8×10^{-6} in. sec.$^{-1}$ to -4.0×10^{-5} in. sec.$^{-1}$ in the case of the 280°C tempered condition), impurity redistribution had no effect on Stage II crack growth kinetics, and retained austenite present in the form of thin films (100-200Å) between martensite platelets or packets decreased the hydrogen-assisted Stage II crack growth rate by two orders of magnitude.

D. Fractography

Optical and SEM fractography confirmed, as found by Gerberich et al,[53] that hydrogen-induced brittle fracture in 4340 steel proceeds by an intergranular fracture path with some plastic deformation evident on the intergranular facets. The extent of the plastic deformation depended on the applied stress intensity (K_{app}) at which the hydrogen-induced cracking occurred as shown in Figure 9. Little plastic deformation appeared at applied stress intensities near K_{th} for any dissolved hydrogen level, but if K_{app} exceeded K_{th} by more than about 5-10 MPa$\sqrt{m}$, a noticeable increase in plastic deformation on the intergranular facets was observed. The amount of plastic deformation on the intergranular facets increased with further increases in K_{app} (see Figure 9).

E. Acoustic Emission

Acoustic emission results were typical of those shown in Figure 17, where the number of emissions is plotted vs. time showing the intermittent nature of hydrogen-induced delayed brittle cracking.

Note that the total acoustic emission from the large grain size specimen (microstructure D) is much greater than that from the small grain size specimen (microstructure F) for the same applied stress intensity range.

DISCUSSION

A. Hydrogen Activity and Mobility

The present investigation has identified three microstructural features which can be utilized to increase the resistance to internal hydrogen-induced delayed cracking in high strength steels. These include trace impurity control, grain size, and the presence and distribution of retained austenite. Discussion of the specific effects of each of these microstructural features on the hydrogen-assisted cracking behavior of AISI 4340 steel necessitates consideration of hydrogen activity and activity gradients in the crack tip region.

Consider a specimen with relatively homogeneous hydrogen distribution. Assume a bulk hydrogen content well above that level at which the baseline K_{th} is first attained but below that hydrogen level above which permanent lattice damage is introduced. In such a specimen containing a sharp notch with no load applied, the activity of hydrogen is a constant (a_H^b) throughout the specimen and no significant activity gradients ($\frac{da_H}{dx}$) of hydrogen exist within the specimen. In general, this means the hydrogen concentration throughout the specimen will also be constant except for small local variations in hydrogen solubility (see Figure 18a).

Upon application of a Mode I load to the specimen, a region of hydrostatic expansion, of a magnitude and extent dependent on the magnitude of the applied stress intensity, is created ahead of the crack tip.

This hydrostatic expansion lowers the local hydrogen activity near the crack tip to a value ($a_H^1(K_{app})$) (Figure 18b) dependent on the magnitude of the hydrostatic expansion forces. This low local hydrogen activity produces an activity gradient and corresponding driving force ($\frac{d\Delta G}{dx}$) for diffusion of hydrogen[86] toward the crack tip region. The driving force for hydrogen diffusion to the crack tip is given by

$$\frac{d\Delta G^D}{dx} = \frac{G_H^b}{x_H^b} - \frac{G_H^{ct}}{x_H^{ct}} = -RT \frac{\ln \frac{a_H^b}{a_H^{ct}}}{dx} \qquad \text{(II)}$$

where "G" is the Gibbs free energy, "R" and "T" have their usual meanings, and the superscript "ct" refers to the crack tip. Under the initial equilibrium conditions, $a_H^{ct} = a_H^b$ and therefore

$$\frac{d\Delta G^D}{dx} = -RT \frac{\ln \frac{a_H^b}{a_H^b}}{dx} = 0 \qquad \text{(III)}$$

However, immediately upon loading, the driving force becomes

$$\frac{d\Delta G^D}{dx} = -RT \frac{\ln \frac{a_H^b}{a_H^1(K_{app})}}{dx} \qquad \text{(IV)}$$

and hydrogen begins diffusing towards the crack tip under the influence of this driving force. This initial driving force (assuming constant temperature) for hydrogen diffusion to the crack tip region and thus the

local hydrogen level ultimately attained, depends on two factors: first, the local hydrogen activity which is determined by the applied stress intensity and second, the bulk hydrogen activity determined by the heat of solution of hydrogen in the microstructure.

As hydrogen diffuses into the region of hydrostatic expansion, the local hydrogen activity increases until equilibrium is achieved; i.e., until $a_H^b = a_H^l$ and thus

$$\frac{d\Delta G^D}{d\ x} = 0 \qquad (V)$$

This results in an increased local hydrogen concentration C_H^l as shown in Figure 18c. Should the critical combination of hydrogen content and applied stress intensity be attained in this localized region, hydrogen-induced cracking will proceed; otherwise, a greater applied stress intensity is required in order to bring more hydrogen to the cracking region. Thus, both the local "equilibrium" hydrogen concentration and the applied stress intensity must increase interdependently until a critical combination is obtained and hydrogen-assisted cracking occurs.

B. Twinning and Grain Size Effects

Oriani[7] suggested that increased grain size might reduce sensitivity to hydrogen-induced cracking of high strength steels by reducing the number and density of possible crack nucleation sites. Several investigators[54,87] have observed increased K_{th} with increased grain size as shown in Figure 19.

With regard to the mechanism of cracking, Troiano[2,4] observed that internal hydrogen cracking initiates ahead of the crack tip as a result of hydrogen diffusion to the triaxial stress points and cracks back to join with the original crack. The process of hydrogen diffusion, crack initiation, and crack jumping then repeats itself. The acoustic emission data shown in Figure 17 supports this model of the cracking mechanism. Therefore, hydrogen-induced delayed brittle failure is predominantly a static, crack initiation phenomenon rather than a dynamic crack growth phenomenon.

Since Troiano's work, it has been observed directly[88] that these hydrogen-induced cracks frequently initiate at grain boundary junctions. The present work has shown (see Figure 9) that hydrogen-assisted cracking in AISI 4340 steel at threshold stress intensity levels was almost wholly intergranular, which implies that any preferred crack initiation sites must lie on the grain boundaries. Thus, the available preferred initiation sites are grain boundary junctions and any inclusion that may lie on or very near the grain boundaries.

The location and extent of the hydrostatic expansion ahead of the crack tip depends on the applied stress intensity as shown schematically in Figure 20. Comparison of fine grain and large grain structures in Figure 20 describes the mechanism by which the threshold stress intensity is determined when only grain size is varied.

Consider first the 15-20 micron grain diameter material in this study loaded at the baseline threshold stress intensity level. The

point of greatest hydrostatic expansion is located at the interface between the plastic zone ahead of the crack tip and the elastically deformed material surrounding it. This location in the fine grain material tempered at 280°C is approximately 0.165 microns ahead of the crack tip. And assuming this crack tip to be at a grain boundary junction and the preferred initiation site to be the nearest nonseparated grain boundary junction ahead of the crack tip, then the greatest hydrostatic expansion is located approximately 3.77 microns away from this preferred initiation site. Thus, in the fine grain material of this investigation, an applied stress intensity of approximately 12 MPa$\sqrt{m}$ was sufficient to produce a driving force great enough to attain a critical combination of stress intensity and hydrogen content at a preferred crack initiation site approximately 3.935 microns ahead of the crack tip (see Figure 20a).

Now consider a large grain (150-200 micron grain diameter) specimen of the same material loaded to the same applied stress intensity of 12 MPa$\sqrt{m}$. The location of the point of greatest hydrostatic expansion remains the same with respect to the crack tip, but note that the nearest preferred initiation site is over ten (10) times as far ahead (approximately 39.10 microns) of the source of the diffusive driving force for hydrogen in this larger grain size material.

Therefore, the driving force for hydrogen diffusion is insufficient to supply the required hydrogen to the preferred initiation site, which is also at a lower applied stress intensity level (see Figure 20b) than the preferred initiation site in the fine-grained material, to produce

the critical combination of stress intensity and hydrogen concentration necessary for crack initiation. A greater applied stress intensity is therefore required in order to attain a critical combination of stress intensity and hydrogen concentration at preferred initiation sites in the large grain size material as shown in Figure 20c.

It is important to note that as the applied stress intensity increases, three factors important to crack initiation are altered: first, the source of the driving force for hydrogen diffusion moves away from the crack tip slightly; second, the magnitude and extent of this driving force for hydrogen diffusion increases; and third, the applied stress intensity at the preferred crack initiation site increases. Therefore, whether the critical stress intensity and the critical hydrogen concentration at the preferred initiation sites in both grain size materials are the same or not cannot be decided conclusively. In either case, baseline threshold stress intensity increases with increasing grain size as long as crack initiation ahead of the crack tip occurs predominantly at these preferred initiation sites, namely, grain boundary junctions.

Although increasing the grain size improved the baseline threshold stress intensity of the AISI 4340 steel, the Stage II crack growth rate characteristics were drastically degraded by increasing grain size. This is easily explained by considering crack jump length and hydrogen diffusion distance.

Note that the concentration profiles in Figure 20 are "equilibrium" hydrogen distributions, but that crack initiation will occur as soon as the hydrogen content at the preferred crack initiation site (c_H^{cis})

reaches the critical level for the corresponding local stress intensity levels above the threshold stress intensity; i.e., in the region of Stage II crack growth. This means that the distance over which the hydrogen must diffuse in either the large grain or fine grain size material is comparable. However, each time a crack initiates and jumps back to the original crack tip, it jumps ten (10) times as far in the large grain size specimen as in the fine grain specimen. This model is supported by two observations in the present study: first, the Stage II crack growth rate for microstructure D (150-200 micron grain diameter) was an order of magnitude greater than that for microstructure F (15-20 micron grain diameter) and the other microstructural features were essentially identical for these two heat treatment schedules. Second, the acoustic emission data in Figure 17 implies that the large grain size material crack jumps release more energy; i.e., trigger more counts per event or crack jump, than the small grain size material. This may partially be due to the higher applied stress intensity near threshold stress intensity levels, but the fact that the distribution of energy appears to be the same throughout the Stage II crack growth range of applied stress intensities implies that the large grain size material simply has a larger crack surface area swept out by each crack initiation and jump back event. Also, the number of counts per event could simply be more sensitive to the size of the crack jumps than to variations in applied stress intensity for the case of crack initiation.

C. Impurity Segregation and Carbide Effects

Phosphorus and sulphur segregated at grain boundaries are known to be embrittling impurities in high strength, low alloy steels.[43,93] In the case of hydrogen-induced cracking, the segregation of phosphorus and sulphur would have the dual effect of lowering the cohesive strength of the grain boundaries[80-84,89] and lowering the activity[5,73] of dissolved hydrogen in the vicinity of the grain boundaries. Lowering the activity of H near grain boundaries leads to increased local solubility for hydrogen as well as an activity gradient to provide a driving force for hydrogen diffusion to the grain boundaries or other areas of phosphorus or sulphur segregation. Thus, phosphorus or sulphur segregation at grain boundaries induces H segregation to grain boundaries, and under the influence of a triaxial stress ahead of a crack tip, less hydrogen is required to diffuse to grain boundaries in the crack tip region than if no phosphorus or sulphur segregation were present. The corresponding attainment of the critical combination of stress intensity and hydrogen concentration required for crack initiation and growth can then occur at a reduced applied stress intensity. The elimination of impurity gradients of phosphorus and sulphur would improve resistance to hydrogen-induced cracking by requiring a larger triaxial stress in order to attain the critical combination of stress intensity and hydrogen concentration ahead of the crack tip.

The effect of reducing the overall impurity content of a steel would be even greater, since it is well documented that both phosphorus

and sulphur are effective recombination poisons enhancing the absorption of hydrogen by iron base alloys.[5,73] Latanison and Opperhauser[88] showed that Sb, another hydrogen recombination poison, segregated at grain boundaries in a nickel 270 alloy and through this poisoning action led to intergranular brittle hydrogen cracking by inducing preferential hydrogen absorption on, and internal hydrogen transport to, grain boundaries. Banerji et al[83] found that by decreasing P from .009 to .003 weight percent, S from .016 to .003 weight percent, and Si from .08 to .002 weight percent, K_{th} increased from approximately 20 MPa$\sqrt{m}$ to approximately 100 MPa$\sqrt{m}$ in a similar 4340 steel. A similar effect was observed by Carter.[87]

Impurities such as phosphorus and sulphur thus present three possible negative influences on resistance to hydrogen-induced delayed brittle fracture of high strength, low alloy steels. First, phosphorus and sulphur produce an embrittling effect on their own when segregated at grain boundaries. Second, the reduced activity of H and resulting solubility increase for H at grain boundaries leads to hydrogen segregation at grain boundaries; and third, an increased susceptibility to hydrogen absorption by the steel occurs due to the action of phosphorus and sulphur as recombination poisons.

The relative homogeneity or segregation of such small amounts of phosphorus or sulphur of concern here would not be expected to significantly affect the mobility and diffusion of hydrogen, and thus Stage II crack growth rates should not be noticeably altered. Comparison of the

Stage II crack growth rates for microstructures A and C or B and D show this to actually be the case.

The effect of the changes in carbide structure between microstructures E and F can help ascertain the mechanism by which hydrogen-induced delayed brittle fracture is affected by microstructure. Increased number and size of carbides decreases the mobility of hydrogen.[58,59,63] Carbides also have a higher solubility for hydrogen than the surrounding metal lattice.[59] And carbides are not known to act as recombination poisons for hydrogen absorption. Carbides apparently do not have an embrittling effect of their own in these microstructures since K_{IC} actually improves with increased number and size of carbides (see Table III) while the yield strength remains constant.

Combining these four statements with the observation that K_{th} was the same for microstructures E and F (see Table IV and Figure 6), it is observed that a trapping mechanism does not explain improved baseline threshold stress intensity values since carbides must act as potential well traps for hydrogen due to their high solubility for hydrogen relative to the metal lattice.

The use of a trapping mechanism does, however, explain reduced crack growth rates since increased trapping would lead to decreased hydrogen mobility and thus to decreased crack growth rates in Stage II. This is observed in comparing Figures 14 and 15 for microstructures E and F where microstructure F exhibits a lower Stage II crack growth rate due to increased number and size of carbides.

D. Effects of Retained Austenite

Khan and Kannan,[79] Thomas,[76] and others[75,78,90] have established that increases in austenitizing temperature for quenched and tempered steel leads to increased quantities of retained austenite in steel, although conflicting evidence has been presented by Ritchie and Horn.[91] Further, it was found [75,79] that the retained austenite was present in the form of thin (100-200 Å) films predominantly along interlath boundaries of the martensitic phase. This finely dispersed distribution of retained austenite would then be ideal for increasing resistance to hydrogen-induced cracking in terms of proposed trapping models.

In the present work, retained austenite apparently acts as a trap for dissolved hydrogen either due to its high solubility for hydrogen relative to the BCC or BCT structure[49,57,92] or due to interfacial accommodation between the FCC and BCC structures.

In either case, the amount of retained austenite present is not sufficient to drastically alter the solubility of hydrogen in the overall microstructure. However, similar to the effects of silicon and manganese on the activity of carbon in mild steel,[93] this fine dispersion of retained austenite does significantly lower the mean effective hydrogen activity (a_H^b) and thus greatly decrease the magnitude of the driving force for hydrogen diffusion to the crack tip region as seen from Equation II. Thus, the required applied stress intensity to produce hydrogen-assisted cracking must increase in order to create sufficient driving force for hydrogen diffusion to produce the critical

combination of applied stress intensity and hydrogen concentration at the crack initiation site.

In addition to increasing the baseline threshold stress intensity as discussed above, the fine platelets of retained austenite also effectively reduce the available diffusional cross-section[62] for hydrogen and thus the rate of hydrogen diffusion toward the crack tip region. This drastic reduction in the hydrogen mobility of the microstructure combined with the decreased relative driving force for hydrogen diffusion leads to the Stage II crack growth rate reduction of two orders of magnitude shown in Figure 16.

The present retained austenite distribution has a dual effect on the hydrogen-induced cracking behavior of AISI 4340 steel. It increases the baseline threshold stress intensity approximately 9 $MPa\sqrt{m}$ by reducing the mean effective hydrogen activity and decreases the Stage II crack growth rate two orders of magnitude by strongly reducing the mobility of hydrogen in the steel matrix. The presence of a fine distribution of retained austenite in quantities great enough to significantly reduce hydrogen activity and mobility but not so great as to detrimentally affect macroscopic mechanical properties is therefore extremely beneficial in terms of resistance to hydrogen-induced delayed brittle fracture of high strength steels.

SUMMARY AND CONCLUSIONS

The hydrogen-induced delayed brittle failure of high strength, low alloy steels is highly dependent on the microstructure produced during heat treatment. Several specific microstructural features significantly alter resistance to hydrogen-assisted cracking: Increased grain size increases both the threshold stress intensity and the Stage II crack growth rate, more homogeneous distribution of impurities such as phosphorus and sulphur increases the threshold stress intensity but hardly affects Stage II crack growth rates, and a fine dispersion of retained austenite platelets greatly improves both threshold stress intensity and Stage II crack growth rate.

From a practical standpoint, both threshold stress intensity and Stage II crack growth rate are important. Higher threshold stress intensities mean improved design capabilities for load-bearing applications under adverse conditions. Slower Stage II crack growth rates allow less frequent integrity checks on service parts operating near design limitations. The plane strain fracture toughness (K_{IC}) must be sufficient to allow crack detection by available techniques; i.e., crack length "a" must be greater than ~ 0.025 inches for practical applications and greater than ~ 0.015 inches under ideal conditions to be detectable. These crack lengths are noted in Figure 16, and as can be seen, only heat treatment A produces a microstructure with the requisite K_{IC} value for practical situations. Also, the Stage II crack growth rate is low enough to allow almost 4.5 hours of lead time between attainment of

crack detectability and catastrophic failure. For example, in testing of aircraft landing gear, this could be significant savings since load-bearing time is relatively short compared to desired lifetimes.

The most significant implication to arise from this study is that any alloy addition or microstructural modification which lowers the bulk activity of hydrogen in a high strength steel while significantly increasing neither the solubility nor the absorption (nor absorption rate) of hydrogen in the alloy should improve resistance to hydrogen-induced delayed brittle fracture. This improvement should be reflected in both decreased baseline threshold stress intensities and reduced Stage II crack growth rates.

Another conclusion is that a trapping mechanism alone cannot explain improved baseline threshold stress intensity, but only reduced Stage II crack growth rates.

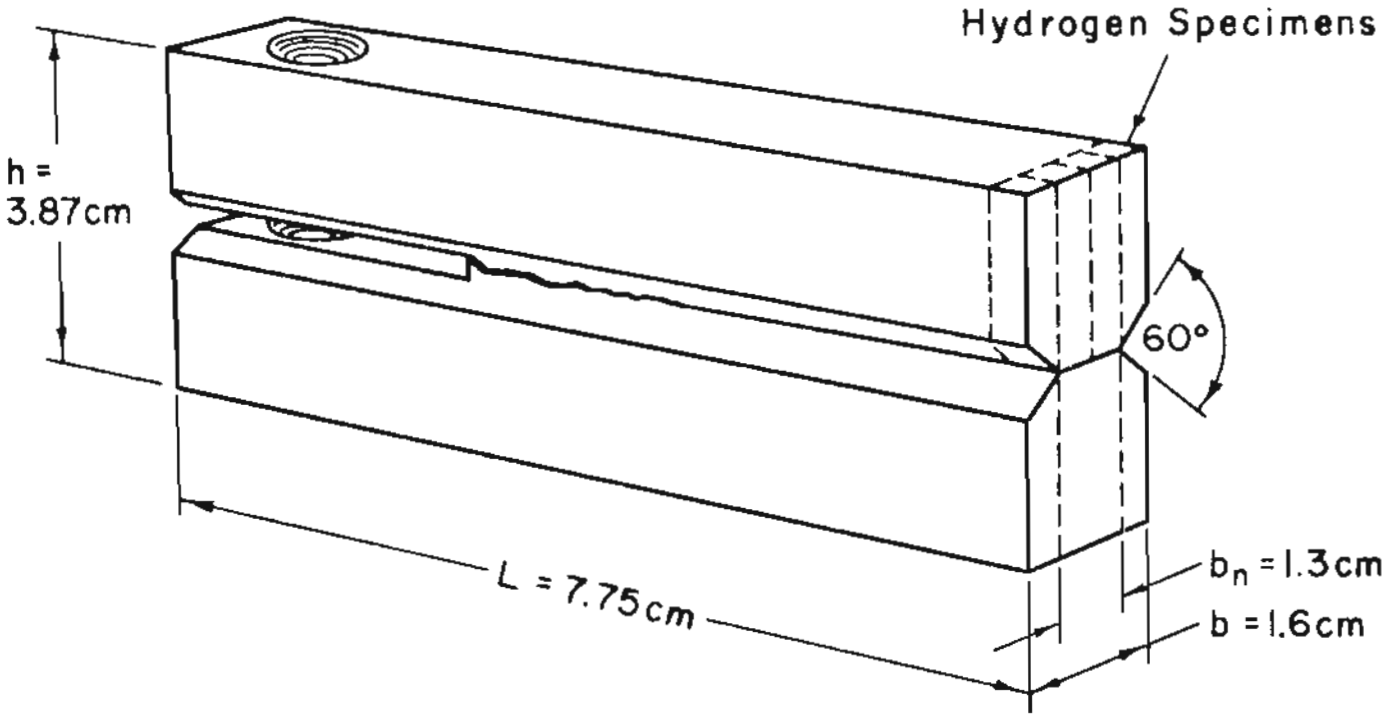

Figure 1. THRESHOLD STRESS INTENSITY SPECIMEN.

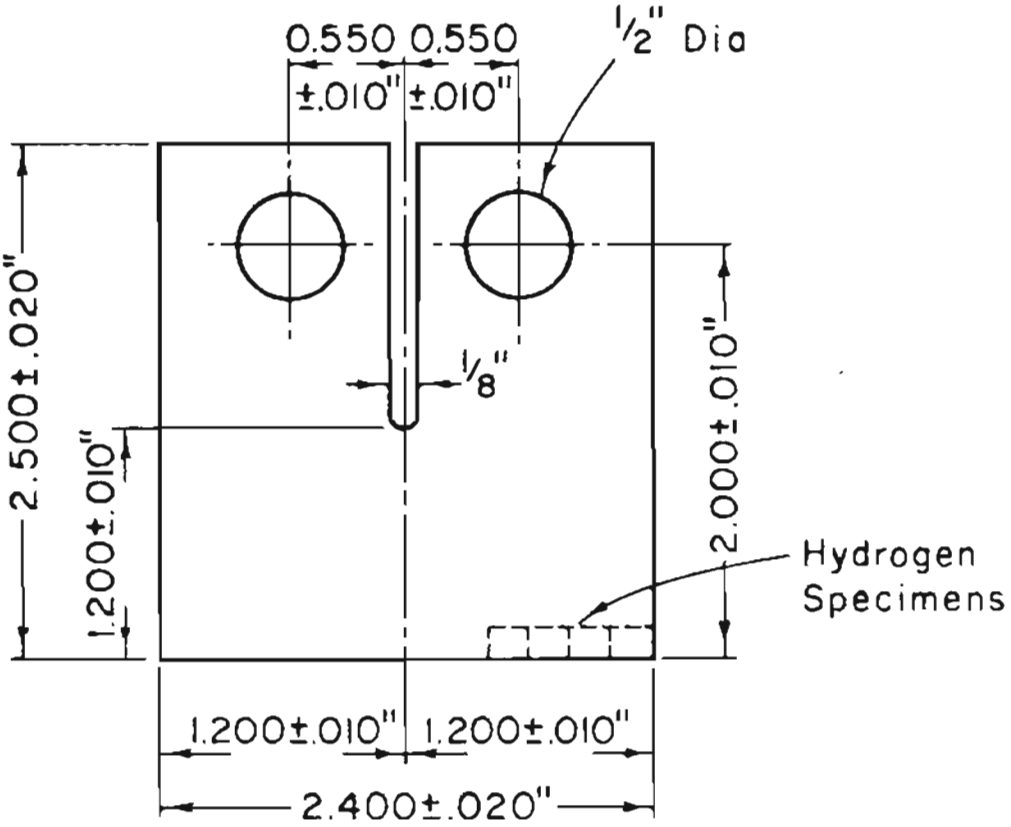

Figure 2. CRACK GROWTH RATE TEST SPECIMEN.

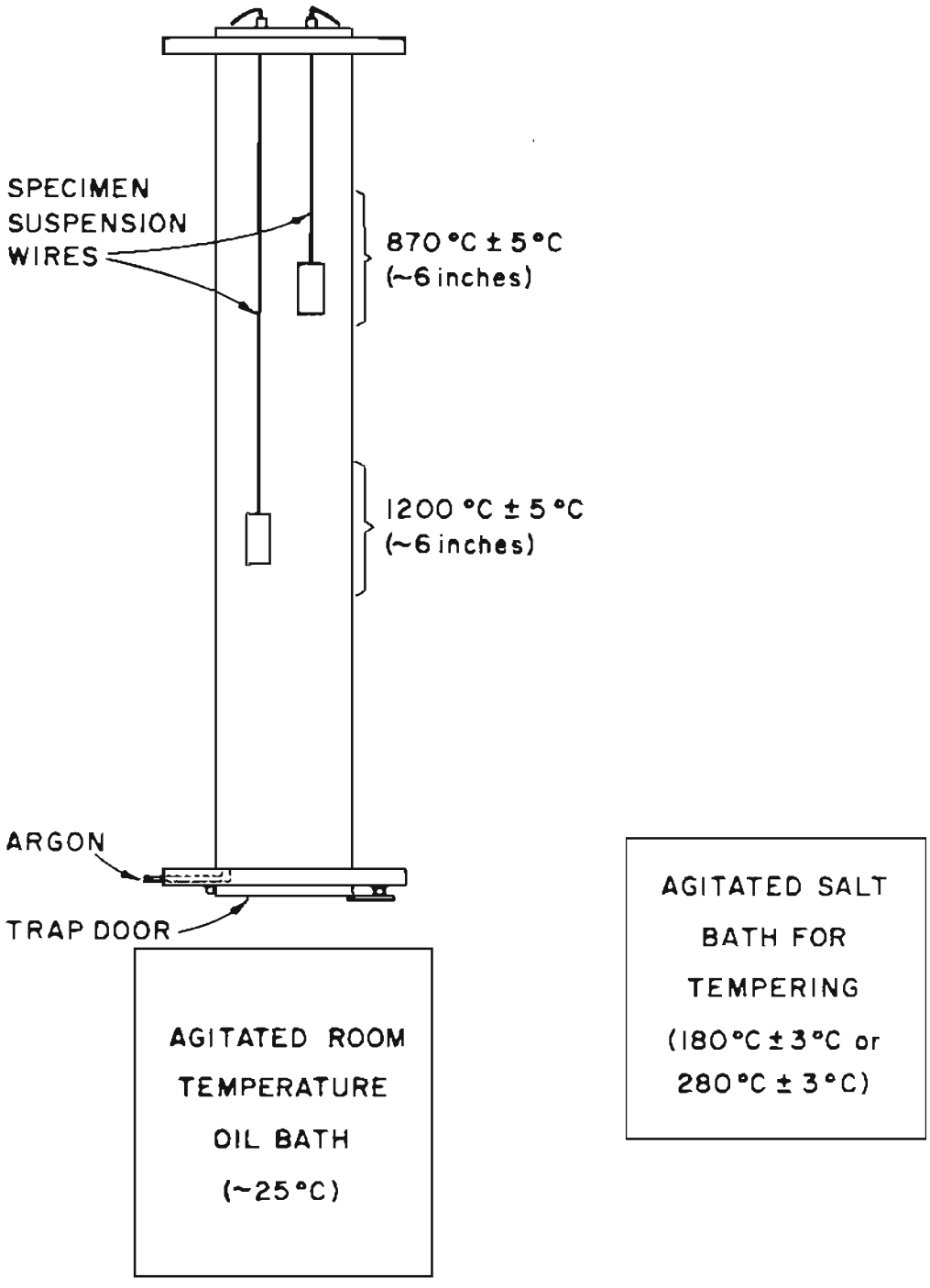

Figure 3. SCHEMATIC OF HEAT TREATING FACILITY.

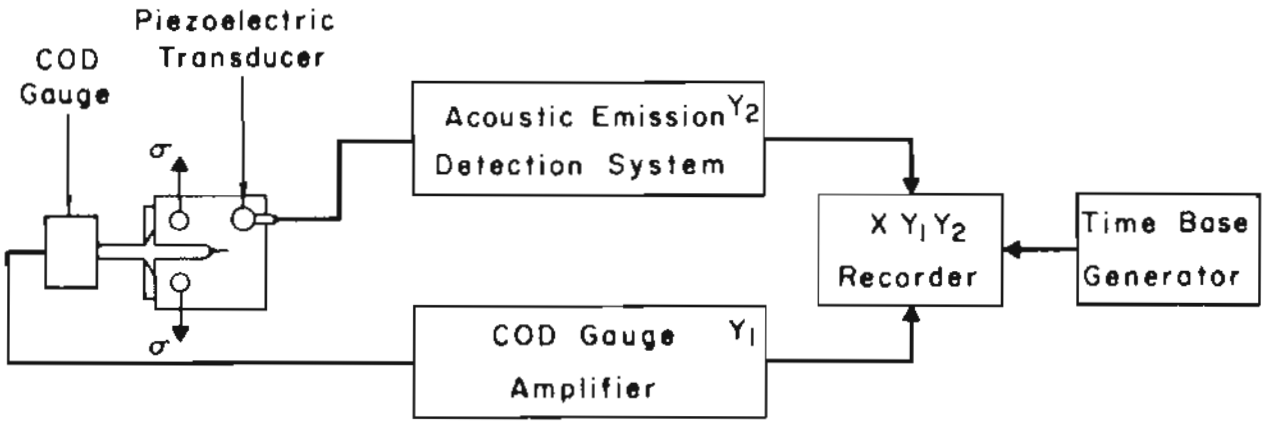

Figure 4. SCHEMATIC OF CRACK GROWTH RATE TEST FACILITY.

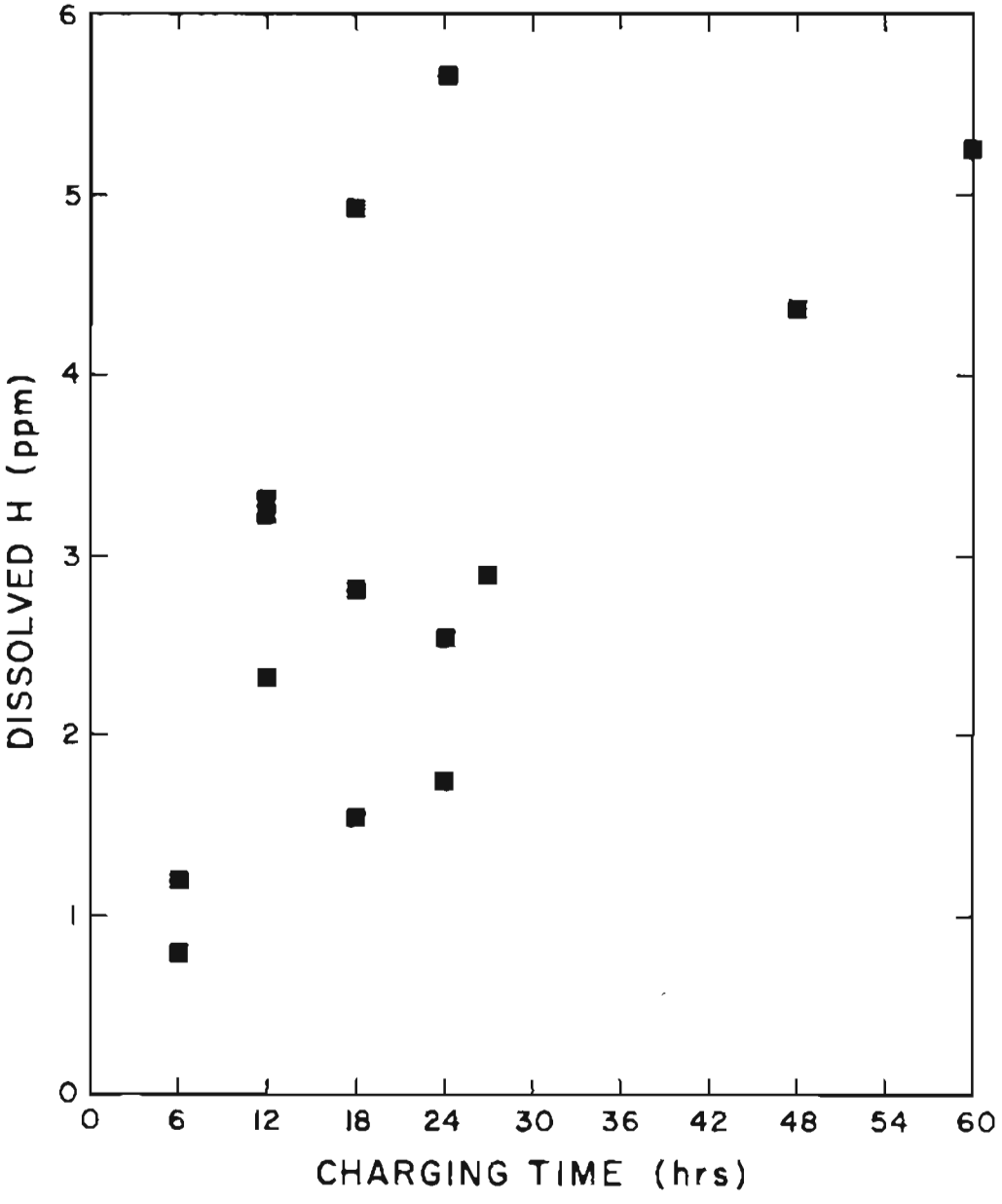

Figure 5. HYDROGEN CONTENT AS A FUNCTION OF CHARGING TIME.

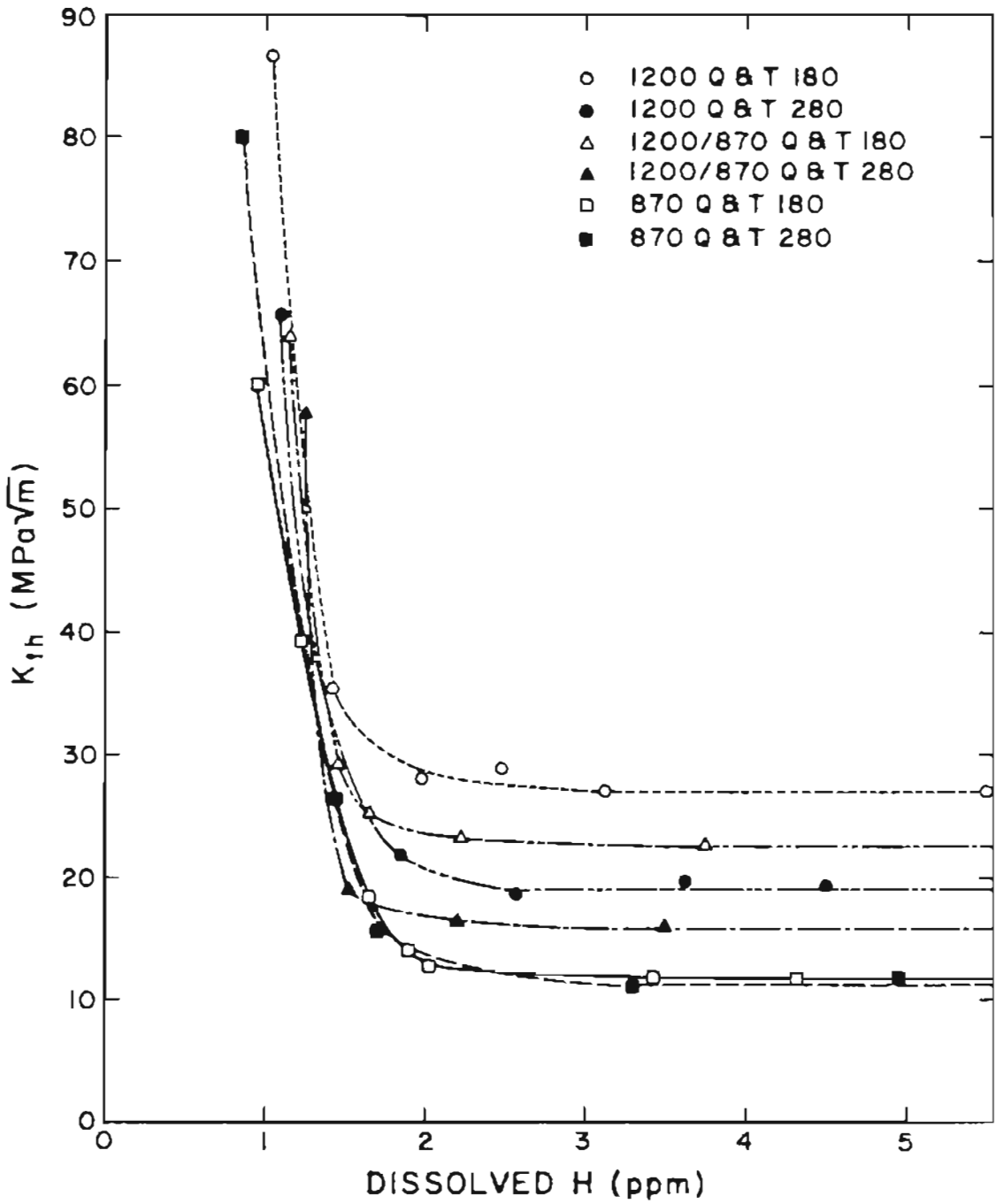

Figure 6. THRESHOLD STRESS INTENSITY AS A FUNCTION OF HYDROGEN CONTENT.

Figure 7. OPTICAL PHOTOMICROGRAPHS SHOWING

a) LARGE (150-200μm) GRAIN SIZE PRODUCED BY 1200°C SOLUTIONING TEMPERATURE,

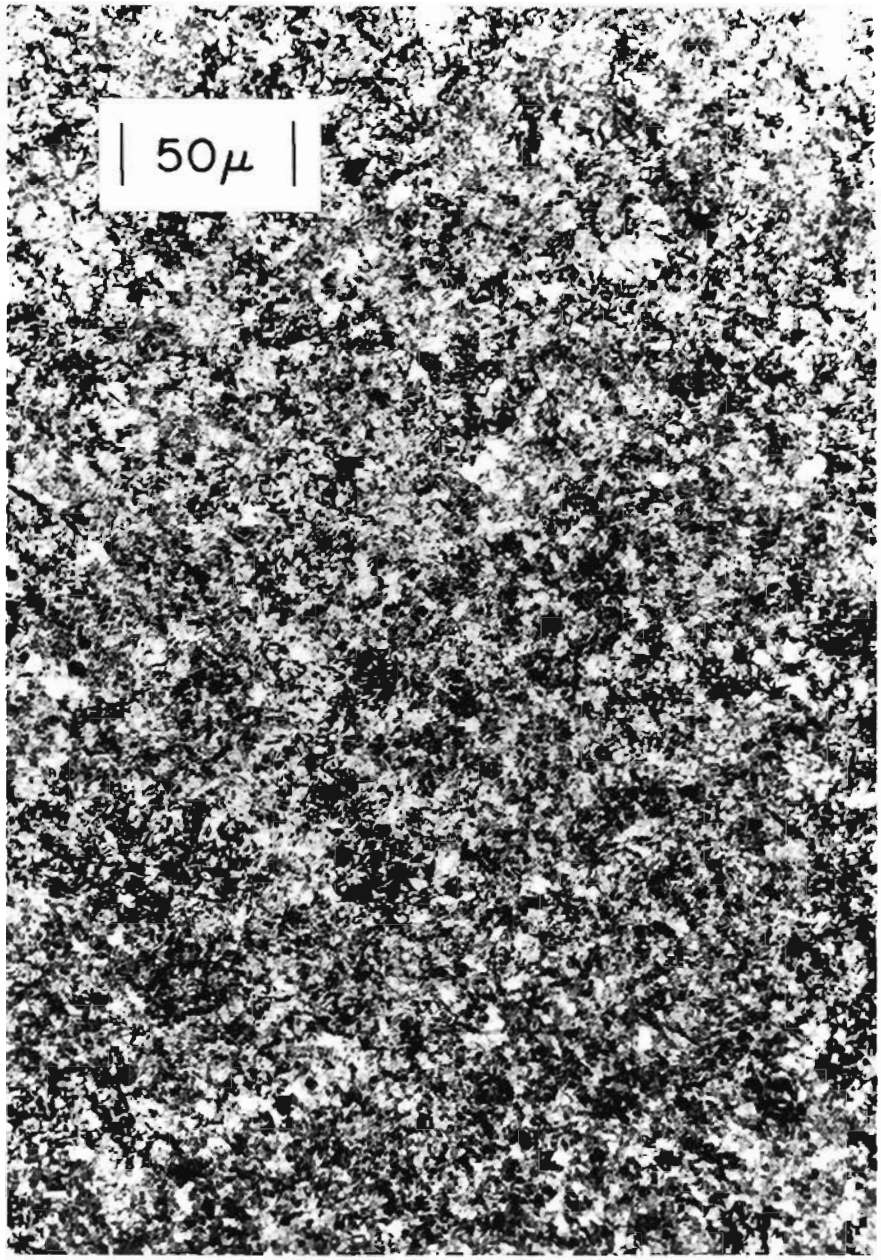

Figure 7. OPTICAL PHOTOMICROGRAPHS SHOWING

(cont.) b) SMALL (15-20μm) GRAIN SIZE PRODUCED BY 870°C SOLUTIONING TEMPERATURE.

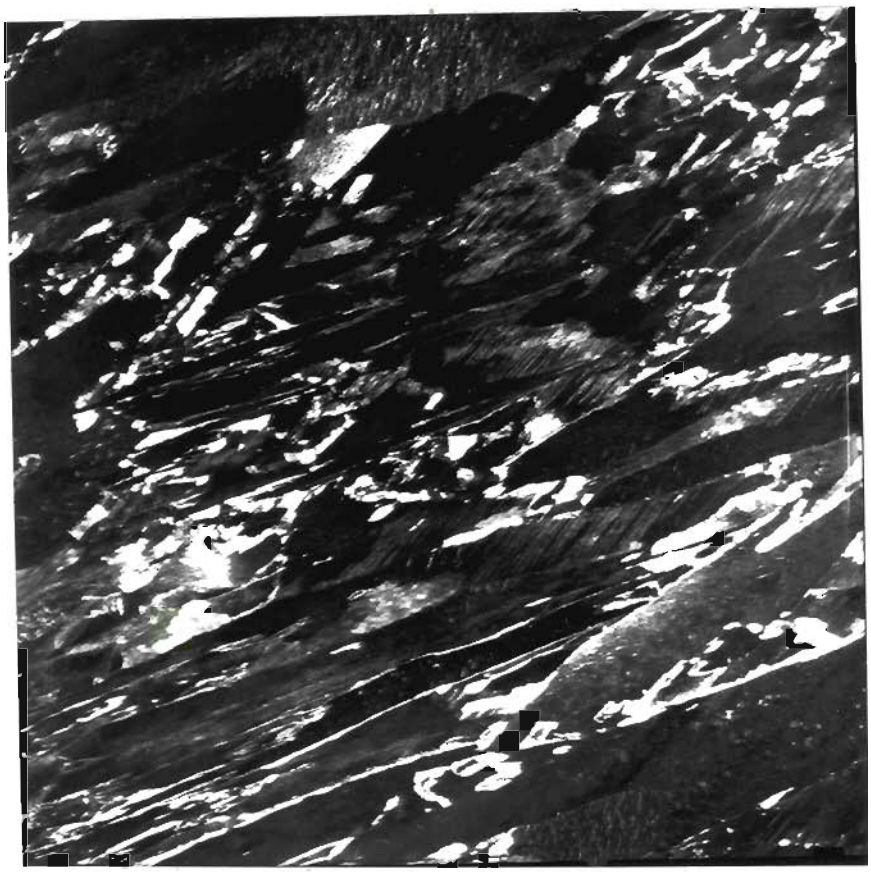

Figure 8. TEM MICROGRAPHS SHOWING

a) PRESENCE OF RETAINED γ IN MICROSTRUCTURE A (ALSO PRESENT IN MICROSTRUCTURE C) AND

Figure 8. TEM MICROGRAPHS SHOWING

(cont.) b) ABSENCE OF RETAINED γ IN MICROSTRUCTURE B ALSO ABSENT IN MICROSTRUCTURE E).

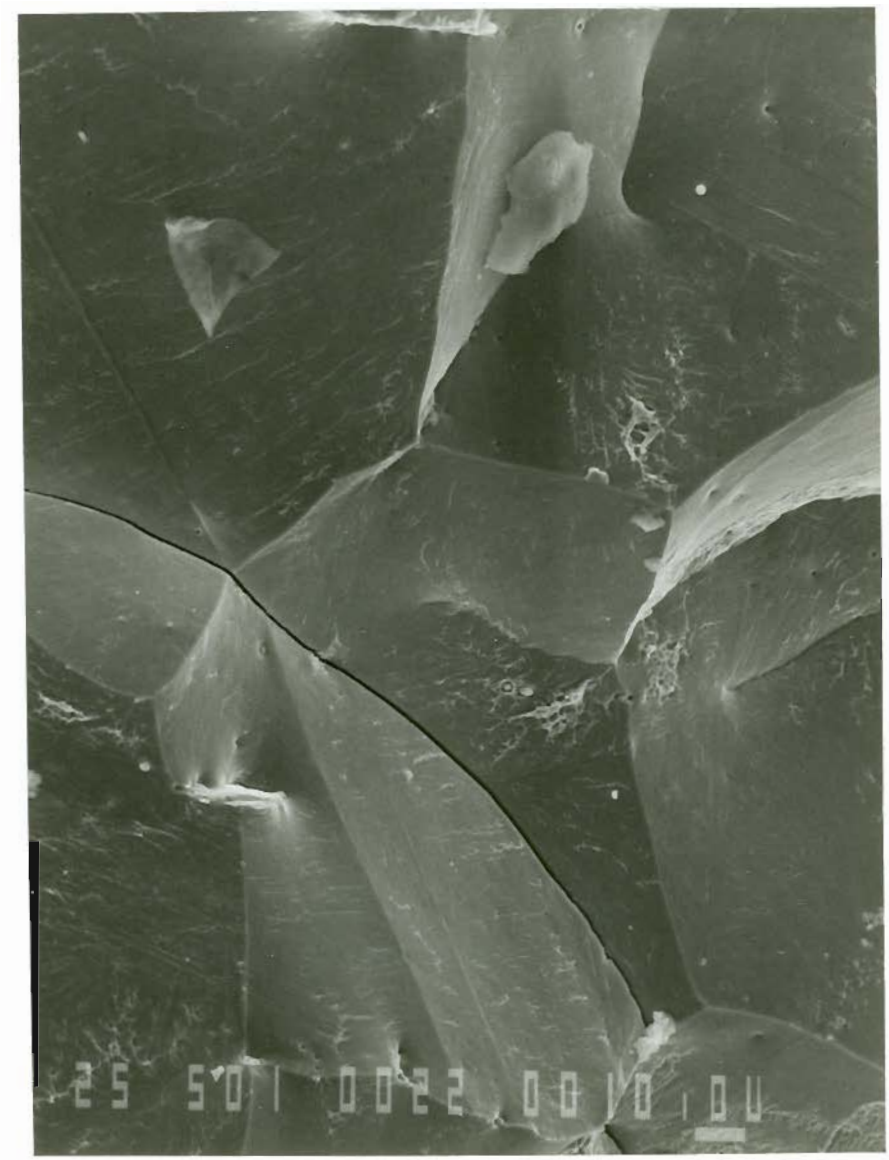

Figure 9. SEM MICROGRAPHS OF HYDROGEN ASSISTED CRACKING FRACTURE SURFACES

a) MICROSTRUCTURE A IN STAGE I CRACK GROWTH REGION ($30MPa\sqrt{m}$)

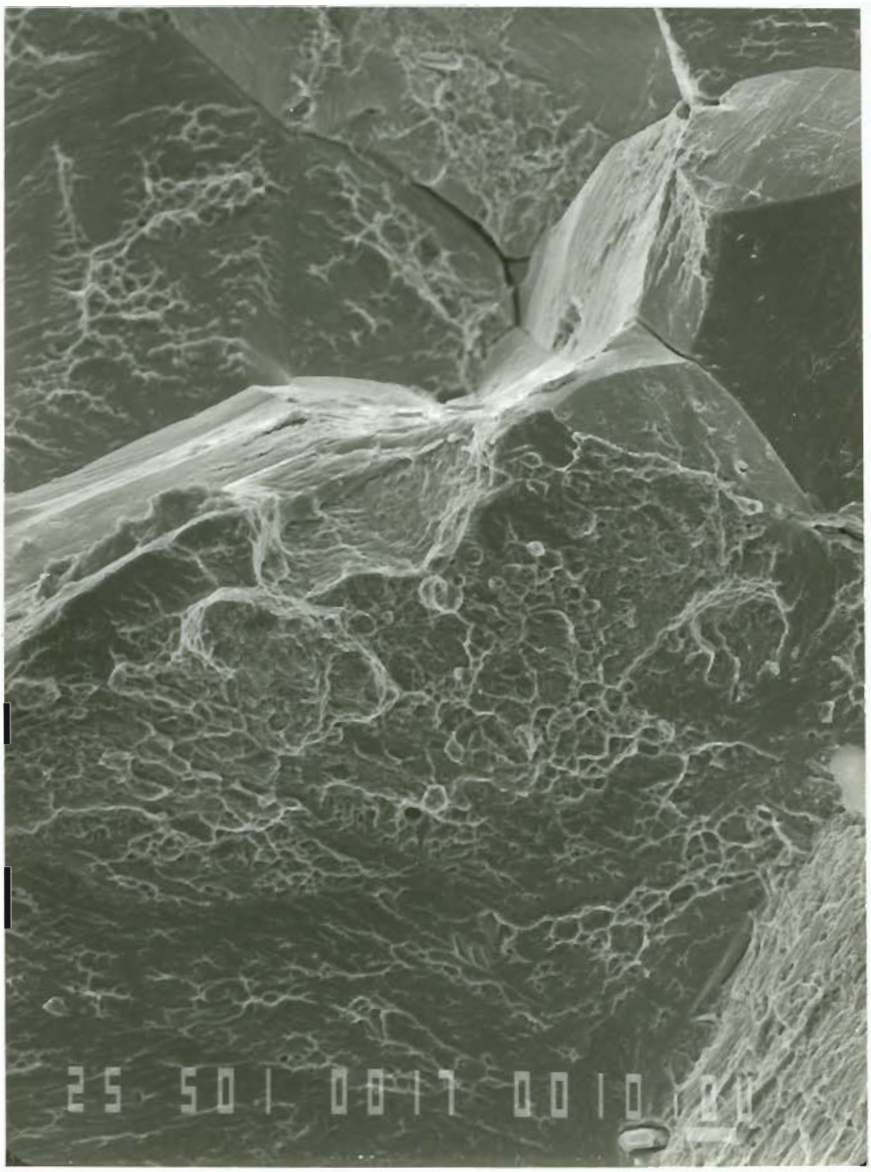

Figure 9. SEM MICROGRAPHS OF HYDROGEN ASSISTED CRACKING FRACTURE SURFACES

(cont.) b) MICROSTRUCTURE A IN STAGE II CRACK GROWTH REGION (55 MPa$\sqrt{m}$)

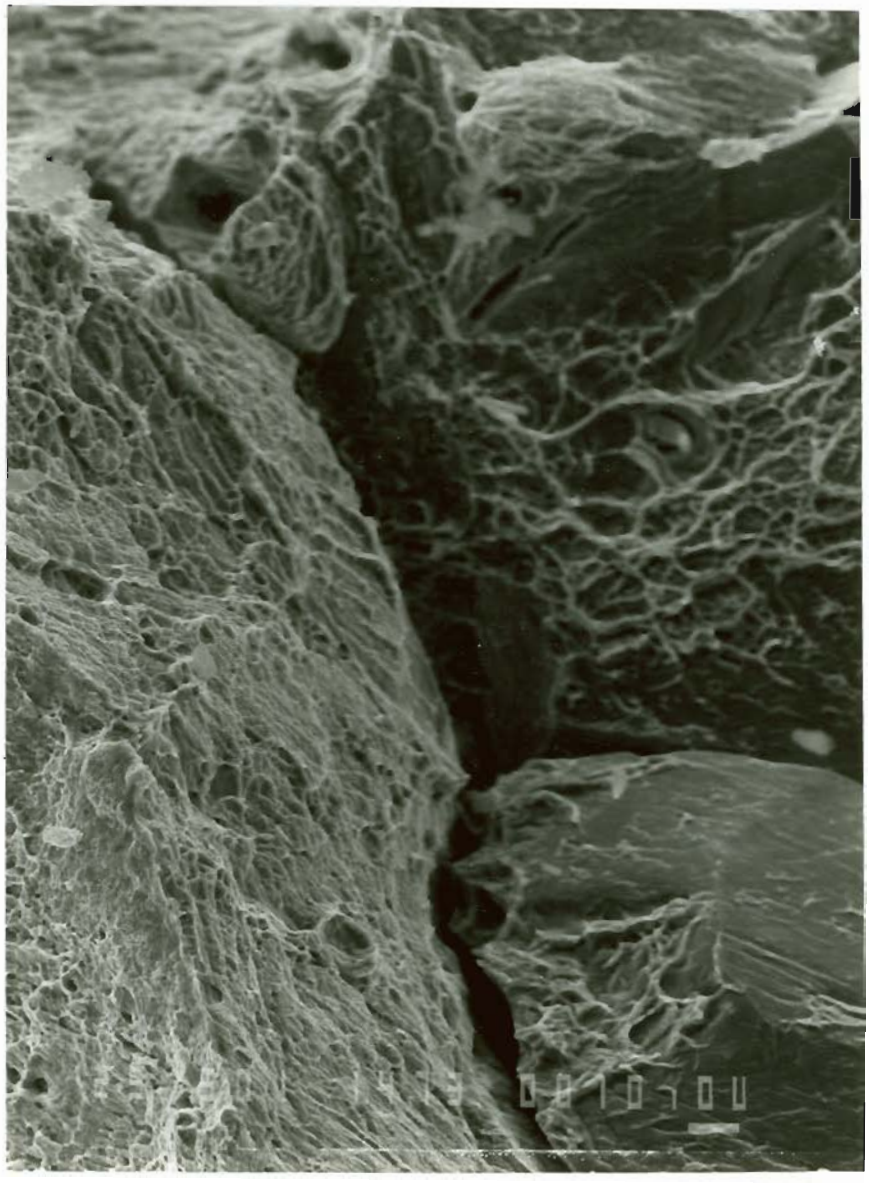

Figure 9. (cont.) SEM MICROGRAPHS OF HYDROGEN ASSISTED CRACKING FRACTURE SURFACES

c) MICROSTRUCTURE A IN STAGE III CRACK GROWTH REGION (90 MPa$\sqrt{m}$)

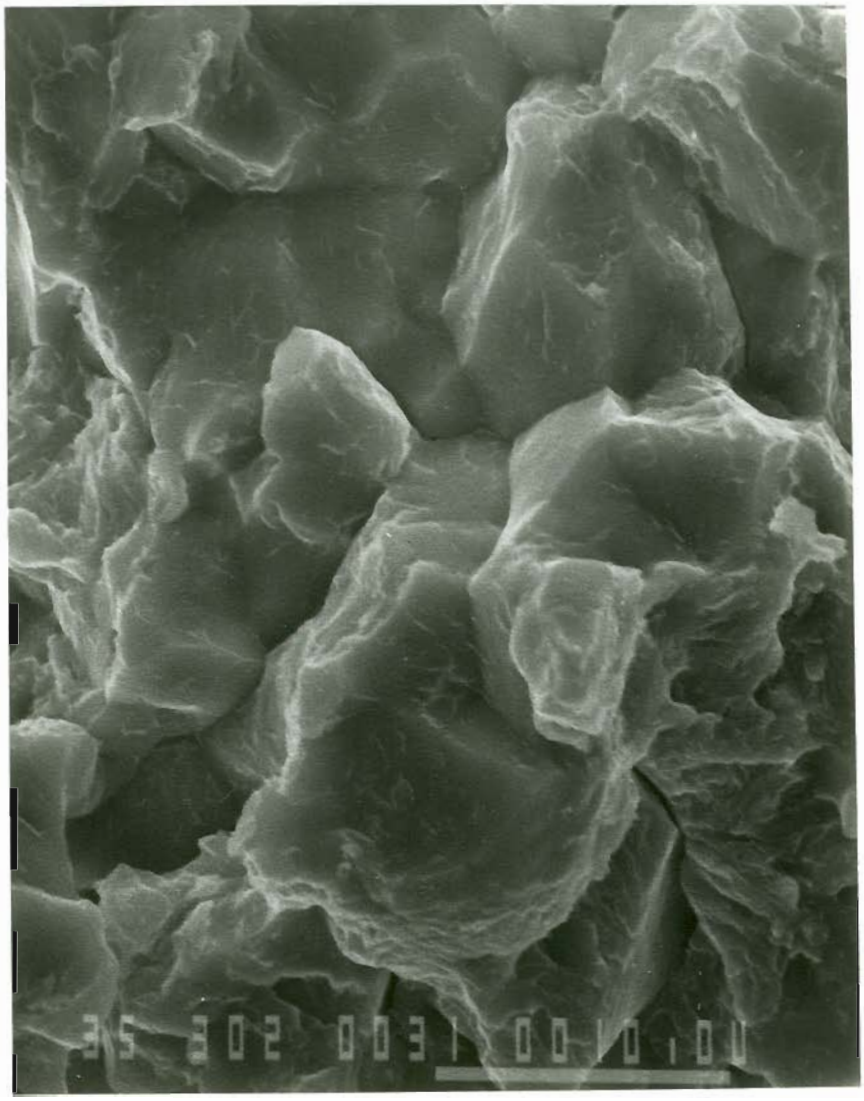

Figure 9. SEM MICROGRAPHS OF HYDROGEN ASSISTED CRACKING FRACTURE SURFACES

(cont.) d) MICROSTRUCTURE E IN STAGE I CRACK GROWTH REGION (12 MPa$\sqrt{m}$)

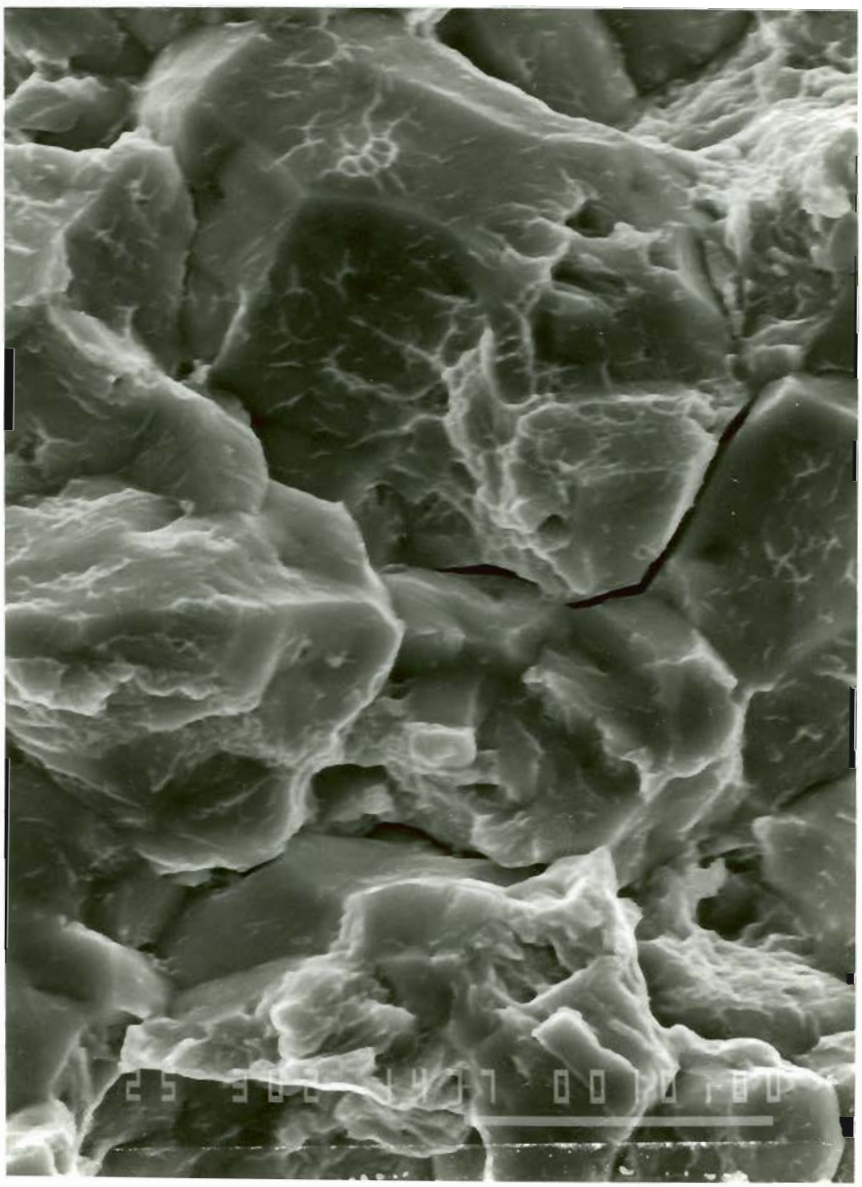

Figure 9. (cont.) SEM MICROGRAPHS OF HYDROGEN ASSISTED CRACKING FRACTURE SURFACES

e) MICROSTRUCTURE E IN STAGE II CRACK GROWTH REGION (30 MPa$\sqrt{m}$)

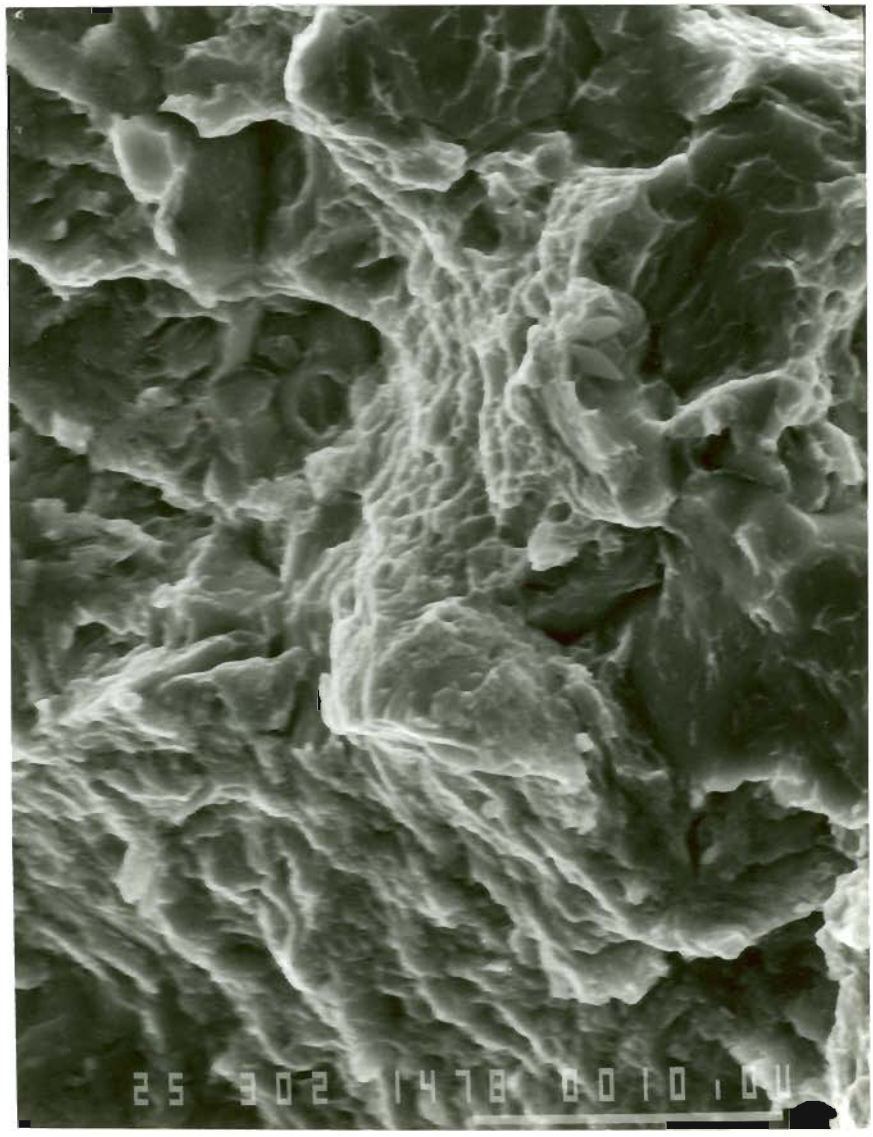

Figure 9. SEM MICROGRAPHS OF HYDROGEN ASSISTED CRACKING FRACTURE SURFACES

(cont.) f) MICROSTRUCTURE E IN STAGE III CRACK GROWTH REGION (55 MPa$\sqrt{m}$).

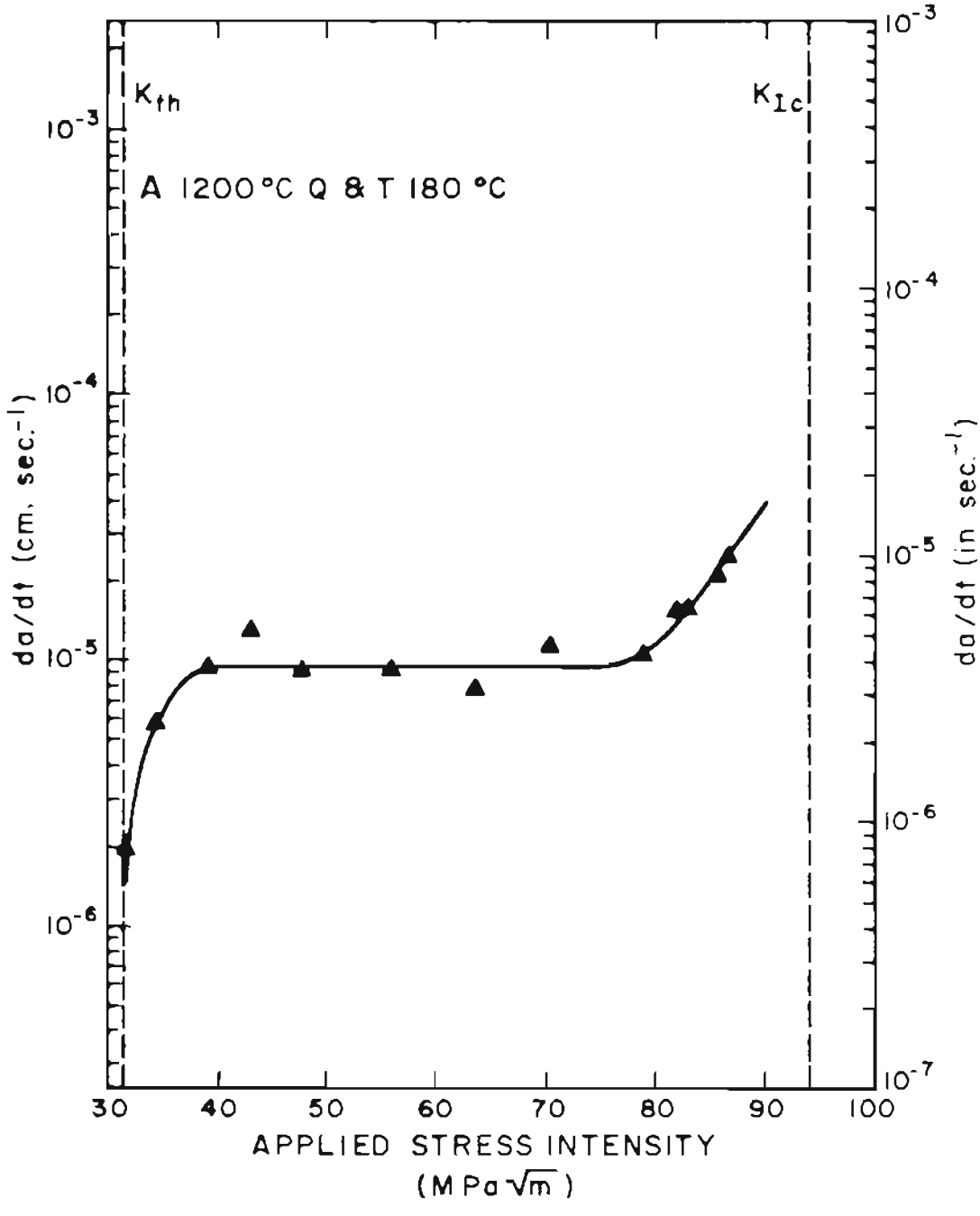

Figure 10. CRACK GROWTH RATE AS A FUNCTION OF APPLIED STRESS INTENSITY FOR MICROSTRUCTURE A.

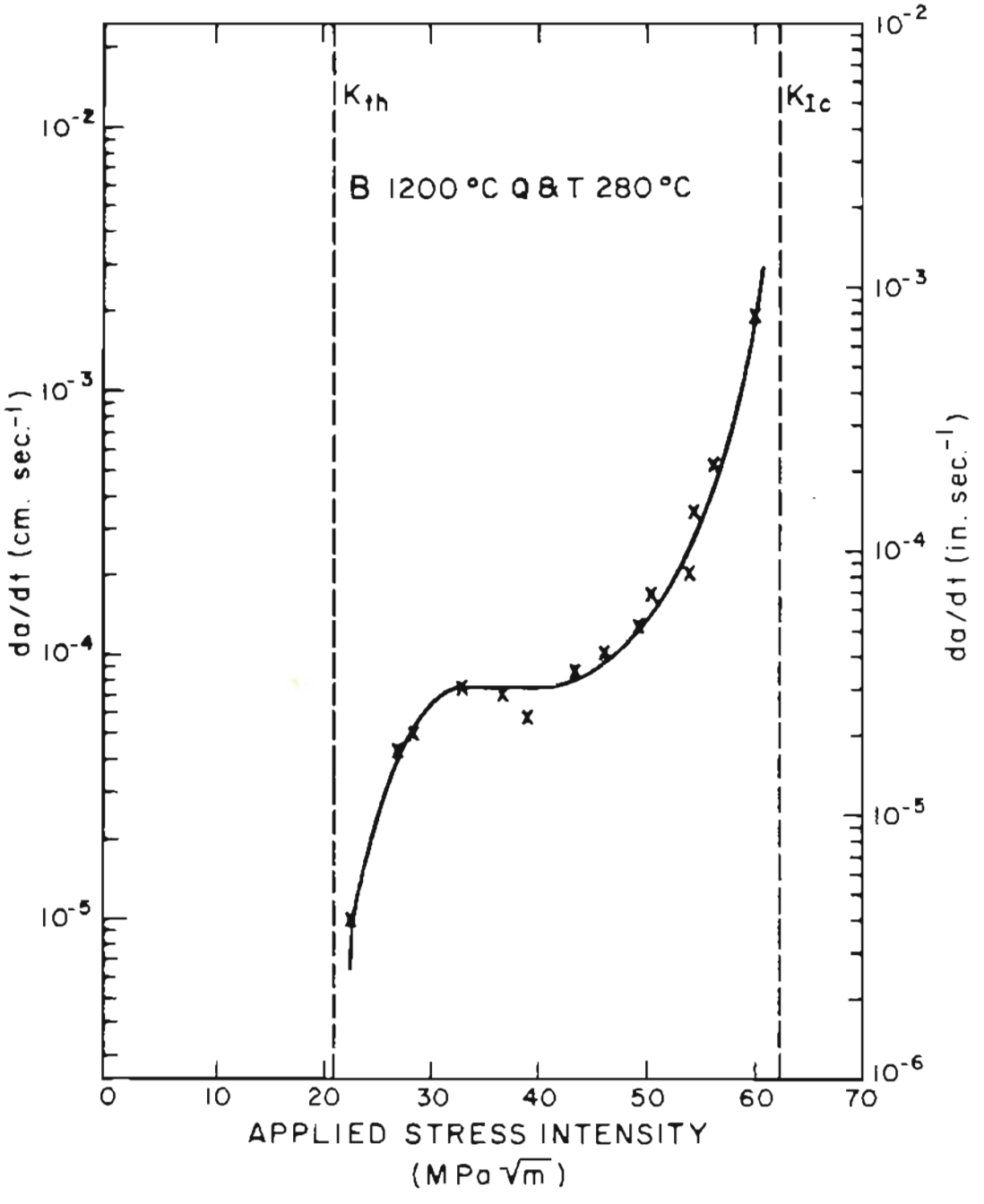

Figure 11. CRACK GROWTH RATE AS A FUNCTION OF APPLIED STRESS INTENSITY FOR MICROSTRUCTURE B.

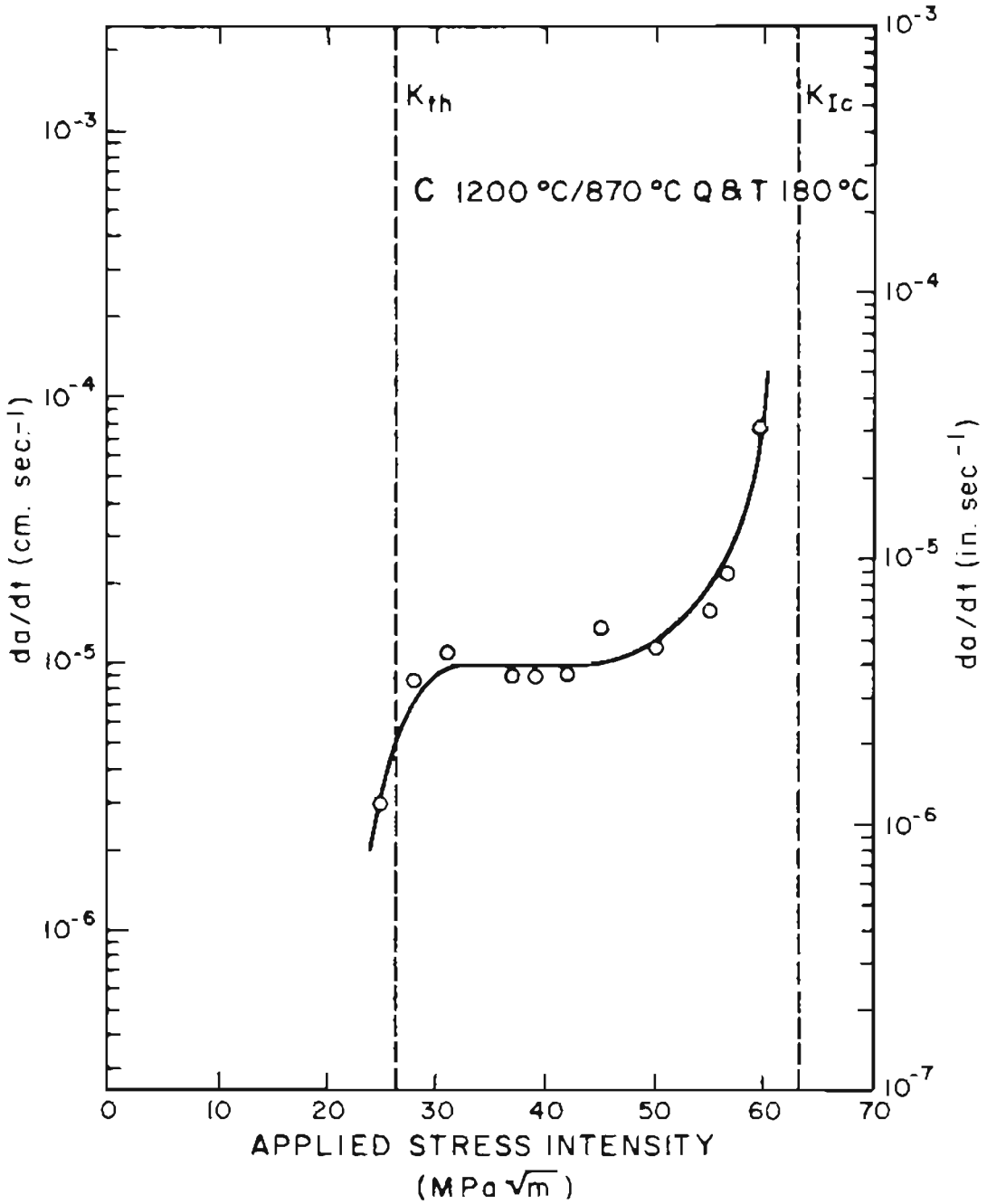

Figure 12. CRACK GROWTH RATE AS A FUNCTION OF APPLIED STRESS INTENSITY FOR MICROSTRUCTURE C.

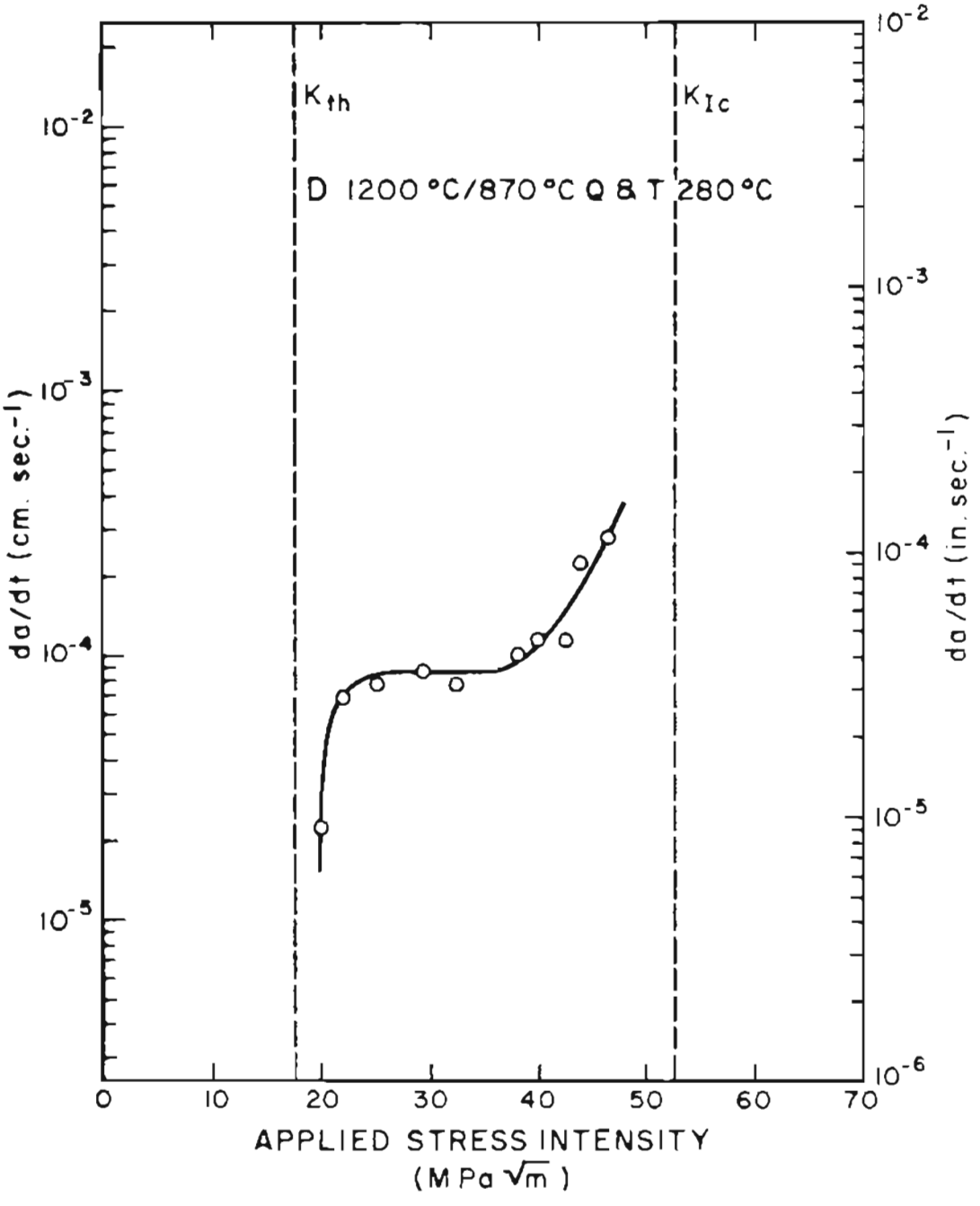

Figure 13. CRACK GROWTH RATE AS A FUNCTION OF APPLIED STRESS INTENSITY FOR MICROSTRUCTURE D.

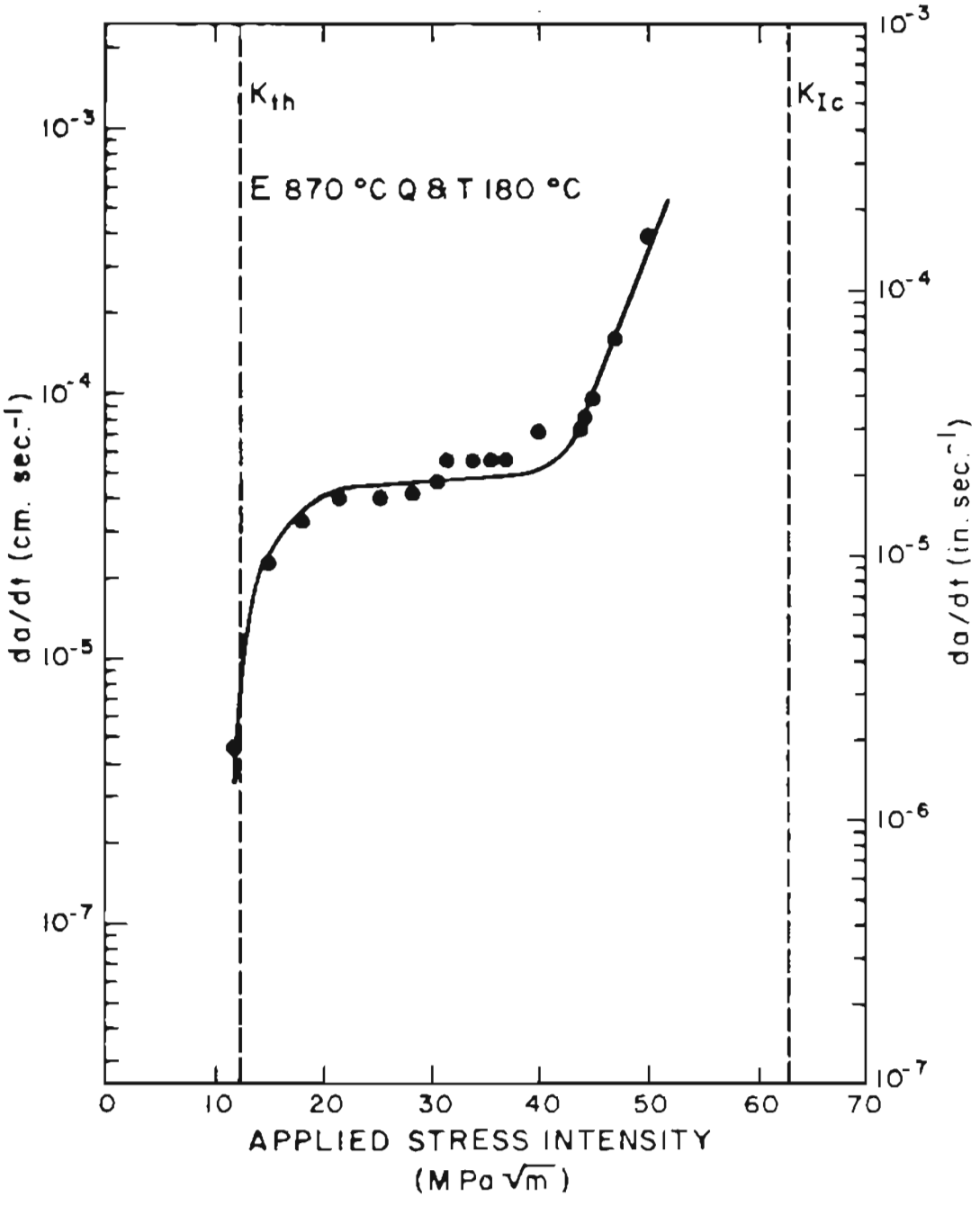

Figure 14. CRACK GROWTH RATE AS A FUNCTION OF APPLIED STRESS INTENSITY FOR MICROSTRUCTURE E.

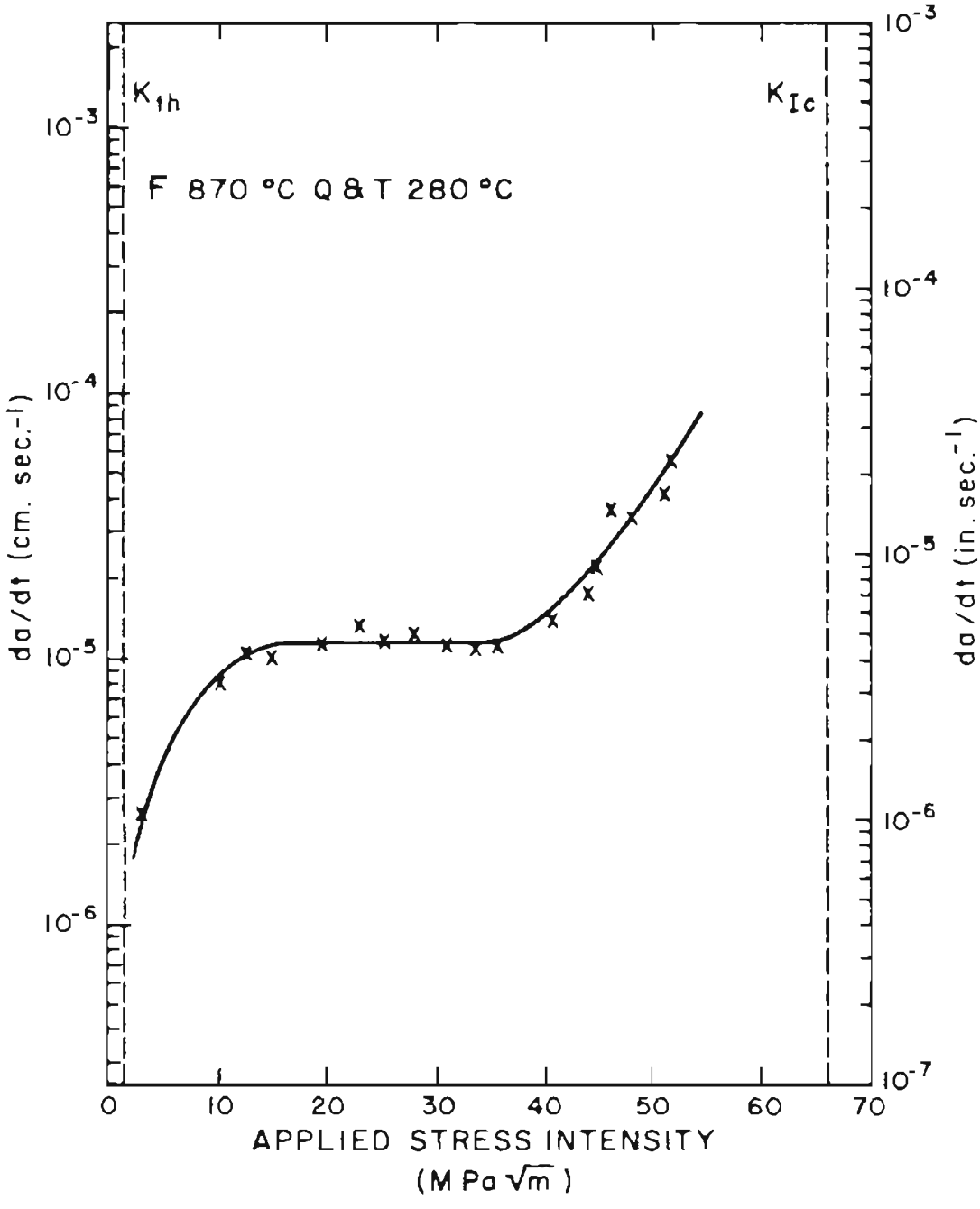

Figure 15. CRACK GROWTH RATE AS A FUNCTION OF APPLIED STRESS INTENSITY FOR MICROSTRUCTURE F.

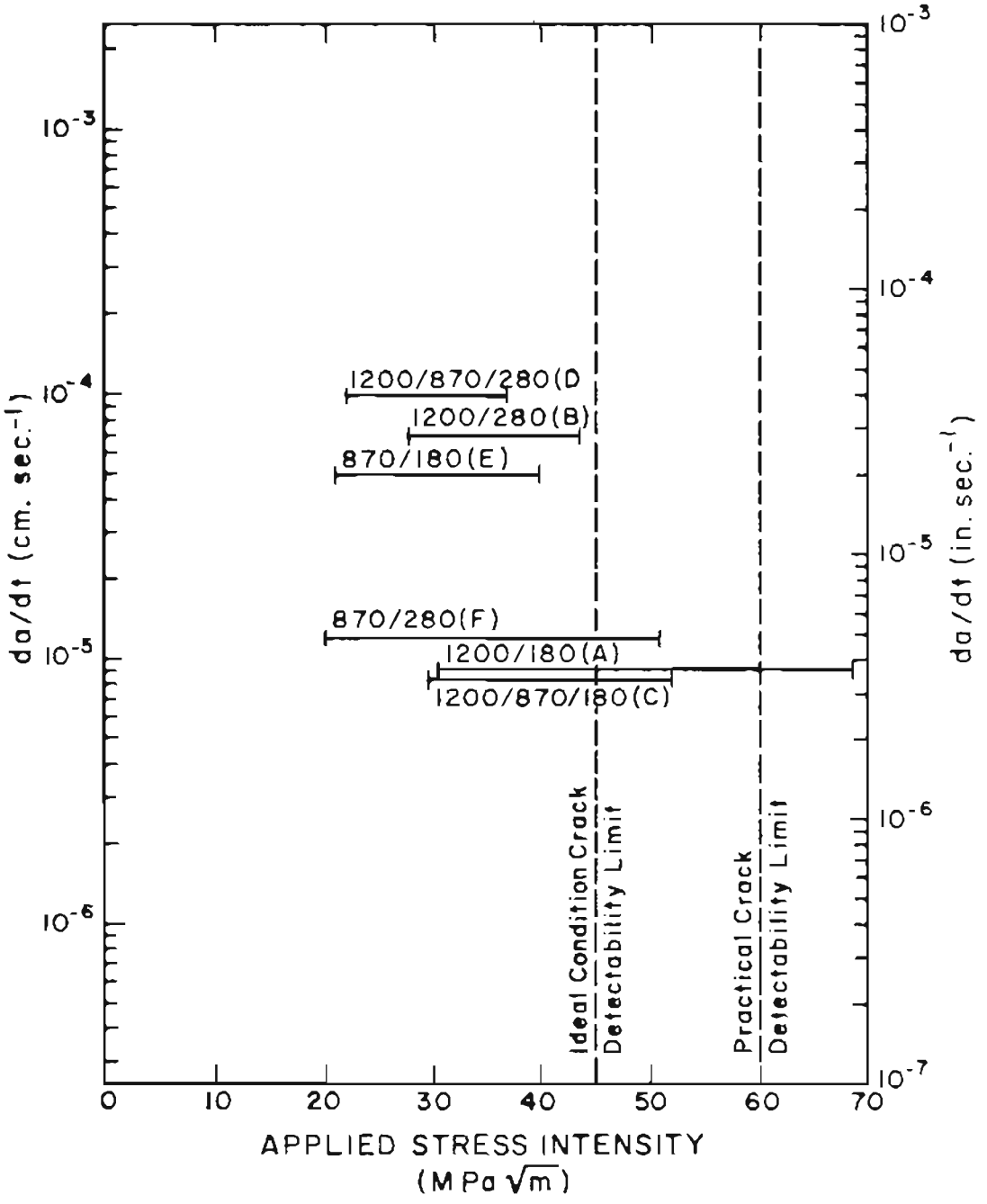

Figure 16. STAGE II CRACK GROWTH RATES AND APPLIED STRESS INTENSITY RANGES FOR ALL MICROSTRUCTURES.

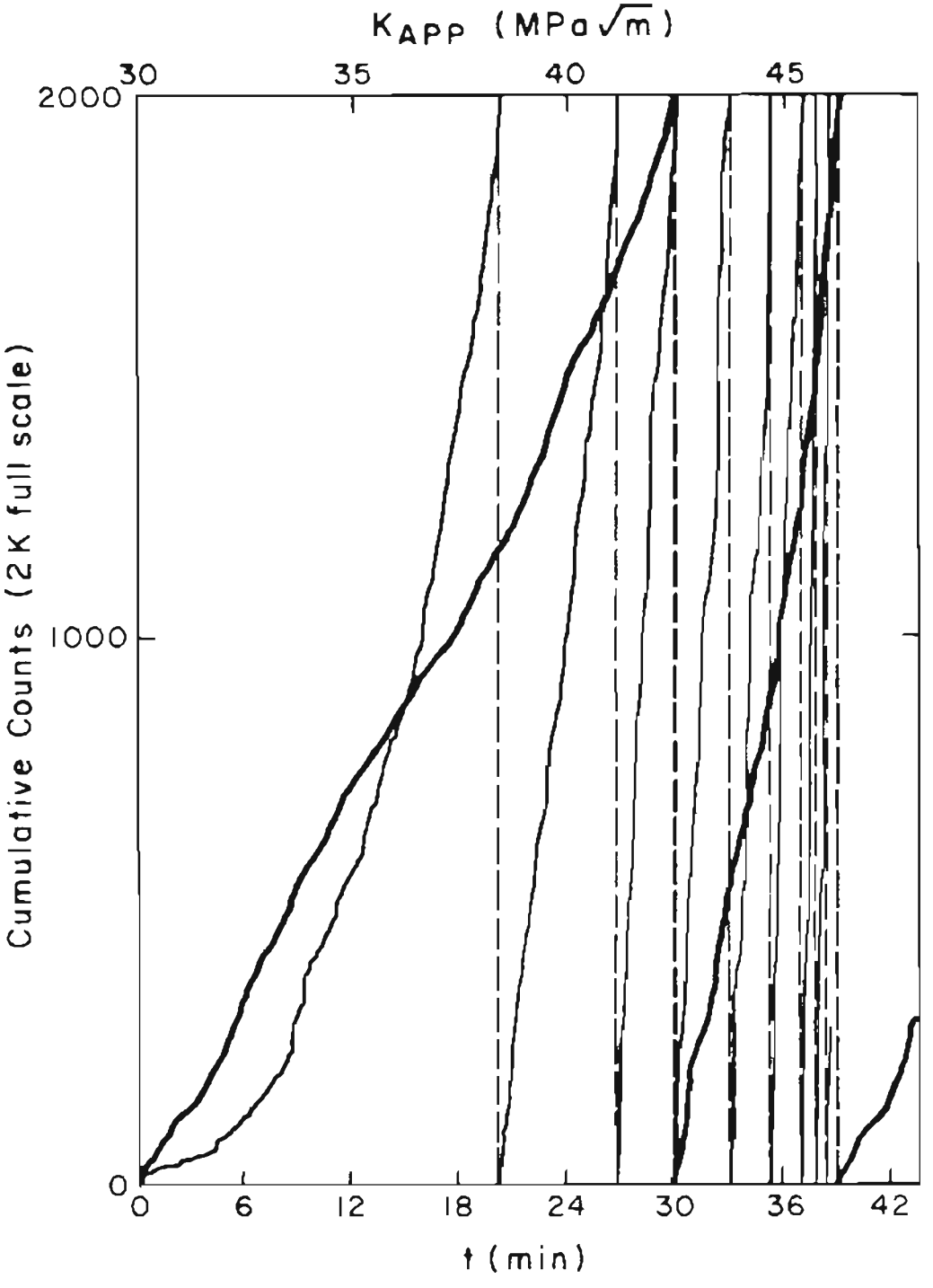

Figure 17. NUMBER OF ACOUSTIC EMISSIONS AS A FUNCTION OF TIME FOR

a) LARGE GRAIN SIZE MICROSTRUCTURE, AND

b) SMALL GRAIN SIZE MICROSTRUCTURE.

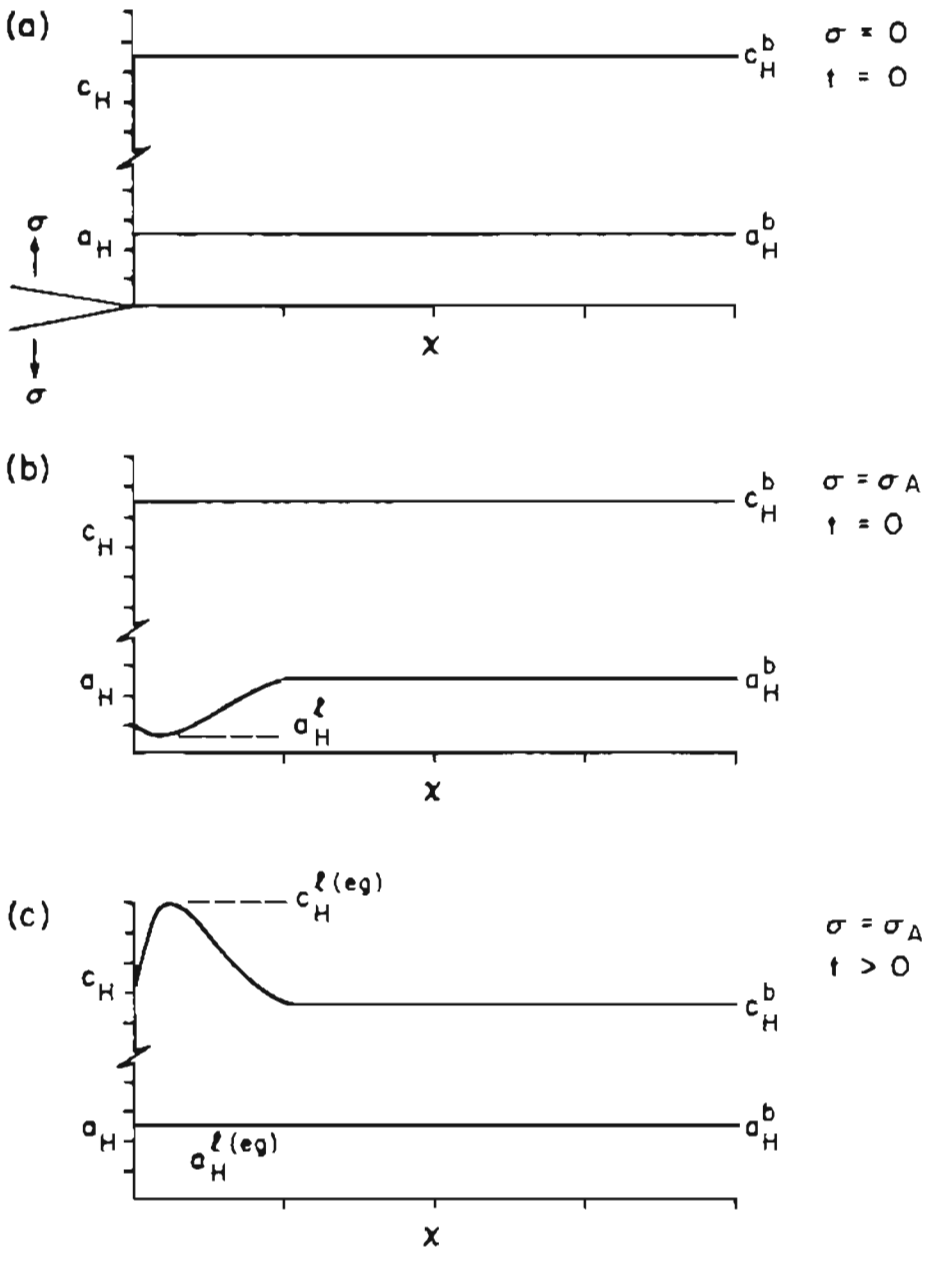

Figure 18. HYDROGEN ACTIVITY AND HYDROGEN CONCENTRATION AS A FUNCTION OF THE DISTANCE AHEAD OF A CRACK TIP

a) BEFORE LOADING,
b) IMMEDIATELY AFTER LOAD APPLICATION,
c) AT SOME TIME t_{eq} AT WHICH "EQUILIBRIUM" HAS BEEN ATTAINED.

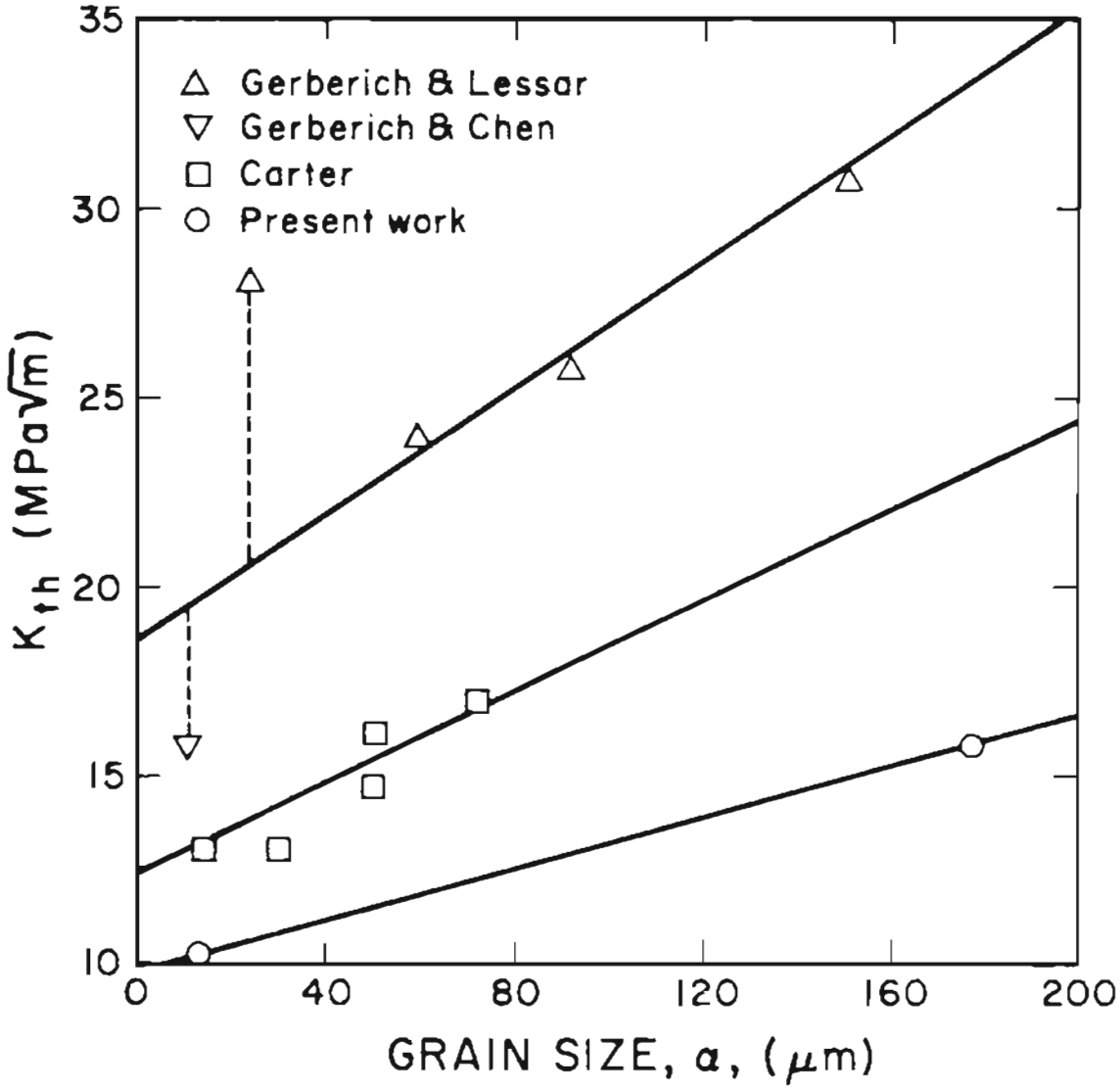

Figure 19. THRESHOLD STRESS INTENSITY AS A FUNCTION OF GRAIN DIAMETER.

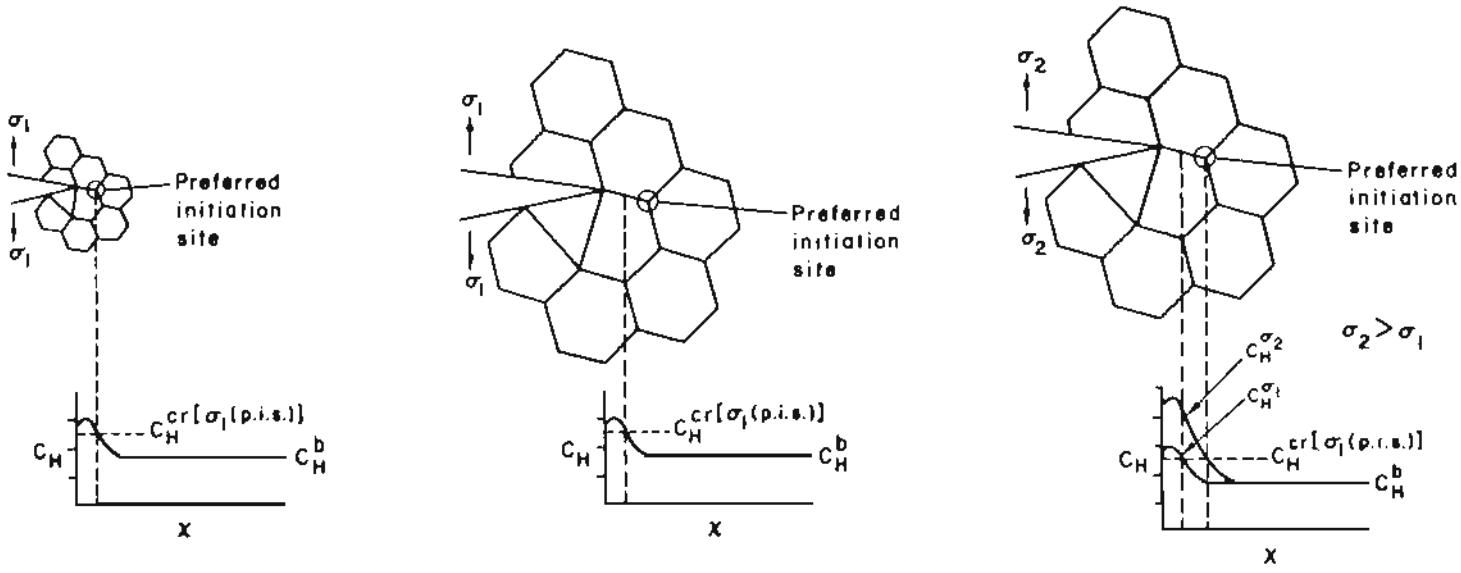

Figure 20. HYDROGEN CONCENTRATION DISTRIBUTION AS A FUNCTION OF DISTANCE AHEAD OF THE CRACK TIP AND ITS RELATION WITH PREFERRED INITIATION SITES AT GRAIN BOUNDARY JUNCTIONS

a) σ_1 ACHIEVES CRITICAL HYDROGEN CONCENTRATION FOR CRACK INITIATION AT PREFERRED INITIATION SITE IN FINE GRAIN MATERIAL,

b) σ_1 IS INSUFFICIENT TO SUPPLY CRITICAL HYDROGEN CONCENTRATION TO PREFERRED INITIATION SITE IN COARSE GRAIN MATERIAL,

c) INCREASED STRESS INTENSITY FROM σ_2 PRODUCES GREATER CONCENTRATION GRADIENT AND SUPPLIES CRITICAL HYDROGEN CONCENTRATION TO PREFERRED INITIATION SITE IN COARSE GRAIN MATERIAL.

TABLE I

Composition of 4340 Alloy

C	Mn	Si	Cr	Ni	Mo	Cu	S	P
.4	.69	.32	.69	1.87	.20	.16	.015	.010

TABLE II

Schedule of Heat Treatments Employed

Heat Treatment	Solution Treatment	Tempering Treatment
A	1200°C 1 hr. oil quench	180°C 1 hr.
B	1200°C 1 hr. oil quench	280°C 1 hr.
C	1200°C 1 hr. furnace quench to 870°C 1/2 hr. oil quench	180°C 1 hr.
D	1200°C 1 hr. furnace quench to 870°C 1/2 hr. oil quench	280°C 1 hr.
E	870°C 1 hr. oil quench	180°C 1 hr.
F	870°C 1 hr. oil quench	280°C 1 hr.

TABLE III

Mechanical Properties and K_{IC} as a Function of Heat Treatment

Heat Treatment	σ_{ys} (MPa)	σ_{ult} (MPa)	Elong.(%)	R.A.(%)	K_{IC} (MPa$\sqrt{m}$)
A	1515	1931	4.5	7.1	99.23
B	1448	1655	1.2	4.5	68.24
C	1526	2069	7.1	13.0	69.50
D	1448	1793	7.3	16.5	57.85
E	1520	2000	13.6	40.2	65.71
F	1517	1655	13.7	53.7	83.84

TABLE IV

Microstructural Features and Mechanical Properties as a Function of the Heat Treatment Variables

Tempering Temperature	SOLUTION TREATMENT		
	1200°C	1200°C/870°C	870°C
	A	C	E
180°C	Retained γ Relatively homogeneous impurity distribution No twinning Grain diameter 150-200μm K_{IC} 99.23 MPa$\sqrt{m}$ K_{th} 39.25 MPa$\sqrt{m}$ σ_{ys} 1515 MPa	Retained γ Grain boundary impurity segregation Extensive twinning Grain diameter 150-200μm K_{IC} 69.5 MPa$\sqrt{m}$ K_{th} 26.5 MPa$\sqrt{m}$ σ_{ys} 1526 MPa	No retained γ Grain boundary impurity segregation Extensive twinning Grain diameter 15-20μm K_{IC} 65.7 MPa$\sqrt{m}$ K_{th} 12.0 MPa$\sqrt{m}$ σ_{ys} 1520 MPa
	B	D	F
280°C	No retained γ Relatively homogeneous impurity distribution No twinning Grain diameter 150-200μm K_{IC} 68.24 MPa$\sqrt{m}$ K_{th} 21.0 MPa$\sqrt{m}$ σ_{ys} 1448 MPa	No retained γ Grain boundary impurity segregation Extensive twinning Grain diameter 150-200μm K_{IC} 57.9 MPa$\sqrt{m}$ K_{th} 17.5 MPa$\sqrt{m}$ σ_{ys} 1448 MPa	No retained γ Grain boundary impurity segregation Extensive twinning Grain diameter 15-20μm K_{IC} 83.9 MPa$\sqrt{m}$ K_{th} 12.0 MPa$\sqrt{m}$ σ_{ys} 1517 MPa

TABLE V

Stage II Crack Growth Rates and Dissolved Hydrogen Contents of Microstructures Studied

Heat Treatment		$\frac{da}{dt}$ (in sec^{-1})	H (ppm by wt)
1200/180	A	3.7×10^{-6}	2.32
1200/280	B	2.8×10^{-5}	2.75
1200/870/180	C	3.4×10^{-6}	3.00
1200/870/280	D	4.0×10^{-5}	2.65
870/180	E	2.0×10^{-5}	2.89
870/280	F	4.8×10^{-6}	3.25

LIST OF REFERENCES

1. J. M. Bernstein, R. Garber, and G. M. Pressouyre, Effect of Hydrogen on Behavior of Materials, ed. Thompson and Bernstein, AIME (1976), p. 37.

2. A. R. Troiano, Trans. ASM 52, 54, (1960).

3. E. A. Steigerwald and G. L. Hanna, "Initiation of Slow Crack Propagation in High Strength Materials."

4. H. H. Johnson, J. G. Morlet, and A. R. Troiano, Trans. Met. Soc. AIME, August (1958), p. 528.

5. E. A. Steigerwald, F. W. Schaller, and A. R. Troiano, Trans. Met. Soc. AIME 218, 832, (1960).

6. J. G. Morlet, H. H. Johnson, and A. R. Troiano, JISI, May (1958), p. 37.

7. R. A. Oriani, Ber. Bunsengens Phys. Chem. 76, 848, (1972).

8. R. A. Oriani, Acta Met 18, 147, (1970).

9. R. A. Oriani and P. H. Josephic, Acta Met 22, 1065, (1974).

10. R. A. Oriani and P. H. Josephic, Acta Met 25, 979, (1977).

11. P. Bastien and P. Azou, Proc. 1st World Met. Cong., ASM, (1951),

12. M. R. Louthan, Jr., G. R. Caskey, Jr., J. A. Donovan, and D. E. Rawl, Jr., Mat. Sci. Eng. 10, 357, (1972).

13. S. P. Lynch and N. E. Ryan, Proc. 2nd Int. Cong. on Hydrogen in Metals, Paris, (1977).

14. J. K. Tien, Effect of Hydrogen on Behavior of Materials, ed. Bernstein and Thompson, Met. Soc. AIME, (1976), p. 309.

15. M. R. Louthan, Jr., Hydrogen in Metals, ed. Bernstein and Thompson, ASM, (1974), p. 53.

16. G. D. Beachen, Met Trans. 3, 437, (1972).

17. N. J. Petch and P. Stables, Nature 169, 842, (1952).

18. C. F. Barth and E. A. Steigerwald, Met. Trans. 1, 3451, (1970).

19. H. H. Uhlig, Phys. Met. of S. C. Fracture, Interscience, (1959).

20. F. de Kazinczy, JISI 177, (1954).

21. C. A. Zapffe and C. E. Sims, Trans. AIME 145, (1941).

22. C. A. Zapffe, Materials and Methods 32, 58, (1950).

23. C. A. Zapffe and M. E. Haslem, Metals Tech. 13, 1, (1946).

24. C. A. Zapffe and C. E. Sims, Metals and Alloys 11, 145, (1940).

25. A. S. Tetelman and A. J. McEvily, Fracture of Structured Materials, Wiley, New York, (1967).

26. H. G. Nelson, D. B. Williams, and A. S. Tetelman, Met. Trans. 2, 1953, (1971).

27. A. R. Elsea and E. E. Fletcher, DMIC Memorandum 180, (1963).

28. A. R. Elsea and E. E. Fletcher, DMIC Report 196, (1964).

29. W. H. Johnson, Proc. Roy. Soc., London 23, 168, (1875).

30. L. B. Pfeil, Proc. Roy. Soc. A112, 182, (1926).

31. J. D. Hobson and C. Sykes, JISI 169, 209, (1951).

32. C. E. Sims, G. A. Moore, and D. W. Williams, Trans. AIME 176, 283, (1948).

33. R. P. Frohnberg, W. J. Barnett, and A. R. Troiano, Trans. AMS 47, 892, (1955).

34. W. A. Bell and A. H. Sully, JISI 178, 15, (1954).

35. E. R. Slaughter, E. E. Fletcher, A. R. Elsea, and G. K. Manning, WADC TR 56-83 (June, 1955).

36. P. Cotterill, Progress in Material Science 9, 205, (1961).

37. A. S. Tetelman, C. N. J. Wagner, and W. D. Robertson, Acta Met 9, 205, (1961),

38. N. J. Petch, Phil Mag. 1, 331, (1956).

39. A. A. Griffith, Phil. Trans. Roy. Soc. London 221A, 163, (1920).

40. A. A. Griffith, Proc. Int. Cong. of App. Mech., Delft, 55, (1925).

41. H. P. Van Leeuwen, Corrosion 32, 34, (1976).

42. H. P. Van Leeuwen, Corrosion 29, 197, (1973).

43. H. P. Van Leeuwen, Corrosion 31, 42, (1975).

44. H. P. Van Leeuwen, Eng. Frac. Mech. 6, 141, (1974).

45. H. P. Van Leeuwen, Eng. Frac. Mech. 9, 291, (1977).

46. D. P. Williams and H. G. Nelson, Met. Trans. 1, 63, (1970).

47. R. A. Oriani, Met. Trans. 1, 2346 (1970).

48. A. S. Tetelman, "The Mechanism of Hydrogen Embrittlement in Steel."

49. M. H. Arnbrusten, J. Am. Chem. Soc. 65, 1043, (1965).

50. E. Lunarska, A. Zielinski, and M. Smialowski, Acta Met 25, 305, (1977).

51. C. St. John and W. W. Gerberich, Met. Trans. 4, 589, (1973).

52. W. W. Gerberich and Y. T. Chen, Scripta Met 8, 243, (1974).

53. W. W. Gerberich, Y. T. Chen, and C. St. John, Met. Trans. 6A, 1485, (1975).

54. J. F. Lessas and W. W. Gerberich, Met. Trans. 7A, 953, (1976).

55. W. W. Gerberich and Y. T. Chen, Met. Trans. 6A, 271, (1975).

56. J. A. Hendrickson, D. S. Wood, and D. S. Clark, ASM preprint 28, (1957).

57. E. E. Fletcher and A. R. Elsea, DMIC Report 219, (1965).

58. F. R. Coe and J. Martin, Met. Sci. J. 3, 209, (1969).

59. A. McNabb and P. K. Foster, Trans. Met. Soc. AIME 227, 618, (1963).

60. R. A. Oriani, Fund. Aspects of SCC, ed. Staehle, Forty, and Van Rooyen, NACE 32, (1967).

61. G. M. Evans and E. C. Rollason, JISI 1591, December (1969).

62. M. Koiwa, Acta Met 22, 1259, (1974).

63. C. S. Kortovich, TRW Tech. Report ER 7814-2.

64. B. D. Craig, Acta Met 25, 1027, (1977).

65. R. O. Ritchie, M. H. C. Cedeno, V. F. Zackay, and E. R. Parker, Met. Trans. 9A, 35, (1978).

66. M. L. Hill and E. W. Johnson, Trans. Met. Soc. AIME 215, 717, (1959).

67. R. Gibala, ASME Abstr. Bull. (Inst. Met. Div.) 1, 36, (1966).

68. L. S. Darken and R. P. Smith, Corrosion 5, 1, (1949).

69. G. Maeser and N. Dautzenberg, Arch. Eisenhuttenw. 36, 175, (1965).

70. M. H. C. Cedeno, Master's Thesis, U. C. Berkeley, (1977).

71. K. B. Das and W. E. Strobelt, U.S. Patent #3783678, (1974).

72. K. B. Das, Hydrogen in Metals, ed. Bernstein and Thompson, ASM, 609, (1974).

73. K. Farrell, Corrosion 26, 105, (1970).

74. Damage Tolerant Design Handbook MCJC-HB-02, Metals and Ceramics Information Center, Batelle, Colorado, (1972).

75. G. Y. Lai, W. E. Wood, R. A. Clark, V. F. Zackay, and E. R. Parker, Met Trans. 5, 1663, (1974).

76. G. Thomas, Met. Trans. 9A, 439, (1978).

77. W. E. Wood, NASC Final Tech. Report N00019-77-C-0135, (1978).

78. K. H. Khan and W. E. Wood, Met. Trans. 9A, 899, (1978).

79. K. H. Khan and V. C. Kannan, 35th Ann. Proc. Electron Microscopy Society Amer., ed. G. W. Bailey, Boston, (1977).

80. T. Ogura, C. J. McMahon, Jr., H. C. Feng, and V. Vitek, Acta Met 26, 1317, (1978).

81. C. J. McMahon, Jr., and V. Vitek, Acta Met 27, 507, (1979).

82. K. L. Moloznik, C. L. Briant, and C. J. McMahon, Jr., NACE 35, 331, (1979).

83. S. K. Banerji, C. J. McMahon, Jr., and H. C. Feng, Met. Trans. 9A, 237, (1978).

84. C. L. Briant, H. C. Feng, and C. J. McMahon, Jr., Met. Trans. 9A, 625, (1978).

85. G. Clark, R. O. Ritchie, and J. F. Knott, Nat. Phys. Sci. 239, 104, (1972).

86. A. Einstein, Ann. Phys. 17 (4), 549, (1905).

87. C. S. Carter, Corrosion 25, 423, (1969).

88. R. M. Latanision and H. Opperhauser, Jr., Met. Trans. 5, 483, (1974).

89. K. Yoshima and C. J. McMahon, Jr., Met. Trans. 5, 363, (1974).

90. J. McMahon and G. Thomas, Proc. Int. Conf. on the Microstructure and Design of Alloys, Cambridge, Vol. 1, 180, Inst. of Metals, London, (1973).

91. R. O. Ritchie and R. M. Horn, Met. Trans. 9A, 331, (1978).

92. R. A. McCoy and W. W. Gerberich, Met. Trans. 4, 401, (1973).

93. L. S. Darken, Trans. AIME 180, 430, (1949).

94. H. G. Nelson, D. P. Williams, and A. S. Tetelman, Met. Trans. 2, 953, (1971).

95. D. P. Doutovich and S. Floseen, Met. Trans. 4, 2627, (1973).

96. F. E. Fiyita, Trans. JIM 17, 232, (1976).

97. G. P. Cherepanov, Eng. Frac. Mech. 5, 1041, (1973).

98. W. A. Van Der Sluys, Eng. Frac. Mech. 1, 447, (1969).

99. W. M. Robertson, Rockwell Int. Publ. SC5052.2FR.

100. P. Doig and G. T. Janes, Met. Trans. 8A, 1993, (1977).

101. R. J. H. Wanhill and P. de Rijk, NLR-TR-73028-U.

102. D. M. Allen-Booth and J. Hewitt, Acta Met 22, 171. (1974).

103. Y. Sakamoto, K. Takao, and S. Tokumitsu, Trans. JIM 18, 603, (1977).

104. Y. Kibuta, K. Sugimoto, S. Ochiai, and K. Iwata, Trans. ISIJ 15, 87, (1975).

105. H. H. Johnson and J. P. Hirth, Met. Trans. 7A, 1543, (1976).

106. T. D. Lee, T. Goldenberg, and J. P. Hirth, "Effect of Hydrogen on Fracture of U-Notch Bend Specimens of Spheroidized 1095 Steel."

107. J. P. Hirth and H. H. Johnson, Corrosion 32, 3, (1976).

108. M. G. Fontana and R. W. Staehle, NTIS AD-A010-265 (1975).

109. W. A. Bell and A. A. Sully, JISI 178, 15, (1954).

110. W. J. Barnett and A. R. Troiano, Trans. AIME 209, 486, (1957).

111. J. B. Seabrook, N. J. Grant, and D. Carney, Trans. AIME 188, 1317, (1950).

112. G. G. Hancock and H. H. Johnson, Trans. Met. Soc. AIME 236, 513, (1966).

113. H. H. Johnson, Proc. Int. Cong. Func. Aspects SCC, NACE 439, (1969).

114. S. P. Lynch and N. E. Ryan, Proc. 2nd Int. Cong. Hydrogen in Metals, Paris, (1977).

115. R. Garber, J. M. Bernstein, and H. W. Thompson, Scripta Met 10, 341, (1976).

116. P. Maulik and J. Burke, Scripta Met 9, 17, (1975).

117. E. G. Famachandran and C. Dasarathy, Acta Met 8, 729, (1970).

118. J. K. Tien, Hydrogen in Metals, ASM (1976).

119. R. P. Brobst and G. Krauss, Met. Trans. 5, 457, (1974).

120. U. V. Bhat and H. K. Lloyd, JISI 165, 382, (1952).

121. M. Smialowski, Hydrogen in Steel. Perganon (1962).

122. M. T. Wang and R. W. Staehle, "Effect of Heat Treatment and Stress Intensity Parameters on Crack Velocity and Fractography of AISI 4340 Steel."

123. F. H. Vitovec, Met. Trans. 8A, 2021, (1977).

PLEASE NOTE:

Page 75 (Vita) missing when material received, and not available from school or from author. Filmed as received.